

# Broad-band ellipsometry study of the anisotropic dielectric response of $\text{YAlO}_3$

Laurent Bugnon, Christian Bernhard, and Premysl Marsik  
*Fribourg University, Fribourg, Fribourg 1700, Switzerland*  
(Dated: March 28, 2024)

We present a broad band (THz to UV) ellipsometry study of the anisotropic dielectric response of the orthorhombic perovskite  $\text{YAlO}_3$ . The ellipsometric measurements have been performed on  $\text{YAlO}_3$  crystals with three different surface cuts and for six high symmetry configurations of the crystal axes with respect to the plane of incidence of the photons. The obtained data are presented in terms of the Mueller Matrix elements  $N$ ,  $C$ , and  $S$  and their features are analyzed and discussed with respect to the anisotropy of the dielectric response tensor. In particular, in the infrared range we have identified all 25 infrared active phonon modes that have been predicted from theoretical studies. We also discuss a negative refraction effect that naturally occurs in the vicinity of an anisotropic longitudinal-optical phonon. Moreover, we have determined the temperature dependence of the phonon parameters between 10 and 330 K. The dielectric response above the phonon range, from about 0.1 to 6.5 eV, is shown to be featureless and characteristic of an insulator with a large band gap above 6.5 eV and is well described by anisotropic Cauchy model.

## I. INTRODUCTION

Yttrium Aluminate ( $\text{YAlO}_3$ , also known as YAP – Yttrium Aluminum Perovskite) can be readily grown as large high quality single crystals. It is transparent in the visible range with a moderate refractive index (of about 1.93) and a small birefringence. The phonon spectrum in the far-infrared range is fairly rich and exhibits a clear anisotropy.  $\text{YAlO}_3$  is also a hard material (Mohs hardness 8.6) with a rather high thermal conductivity. For some of those qualities, it has been proposed as a material for hosting lasing dopants [1–3], as alternative for the well-known yttrium-aluminum-garnet  $\text{Y}_3\text{Al}_5\text{O}_{12}$  (YAG).

$\text{YAlO}_3$  is also frequently used as a substrate for the epitaxial growth of thin films from unconventional oxides. In particular, the lattice parameters of  $\text{YAlO}_3$  are well matched with those of several interesting perovskite manganites and their anisotropy can be utilized for the tailored growth of strain-engineered samples [4, 5]. The aim of the present work is to lay the ground for the optical spectroscopy of such thin films and heterostructures which require a detailed a-priori knowledge of the anisotropic response of the  $\text{YAlO}_3$  substrate.

The Raman response of  $\text{YAlO}_3$  has been already studied in great detail [6–10]. Theoretical studies of the IR and Raman phonon spectra of  $\text{YAlO}_3$  have also been reported [7, 10–12]. However, the corresponding detailed optical studies of the IR dielectric tensor and the anisotropy of the phonon response are still missing.

Infrared spectroscopic ellipsometry has proven to be an excellent technique for studies of the phonon response of ionic crystals [13], especially of those with a strong optical anisotropy. For isotropic bulk materials, ellipsometry allows one to directly measure the complex dielectric function. Unlike IR reflectivity measurements which probe only the amplitude of the reflected signal (but not the phase), it does not require a Kramers-Kronig transformation and the related extrapolation of the data to zero and infinite frequency.

For anisotropic crystals, the interpretation of the el-

lipsometry spectra is more complicated since the probing light interacts with the sample under general angle of incidence and polarization state. In general, the measured spectra can be affected by all the elements of the dielectric tensor. In such cases, several ellipsometry measurements must be performed on different surfaces and for various orientations of the crystal axes with respect to the plane of incidence and the combined data need to be analyzed with an anisotropic model that allows for finite diagonal and off-diagonal elements of the dielectric tensor. For materials with tetragonal or orthorhombic symmetry, this can be done on high symmetry cuts [14–17] or with a sequence of different orientations of single low-symmetry cut crystal [18].

In the following, we present a broad-band (THz to UV) ellipsometry study of the dielectric tensor of orthorhombic  $\text{YAlO}_3$ . The measurements are performed on crystals with high symmetry surface cuts and for high symmetry orientations of the crystal axes with respect to the plane of incidence of the photon beam. We present a detailed analysis of ellipsometric data of all 6 high symmetry configurations and document the temperature dependence of the  $\text{YAlO}_3$  phonon parameters.

## II. SAMPLES AND EXPERIMENT SETUPS

$\text{YAlO}_3$  crystallizes in a distorted perovskite structure with orthorhombic symmetry as displayed in Fig. 1a. Using the Pbnm notation, the orthorhombic lattice parameters are  $a = 5.18 \text{ \AA}$ ,  $b = 5.33 \text{ \AA}$  and  $c = 7.375 \text{ \AA}$  [19, 20]. Throughout the manuscript, we will use the notation  $a$ -,  $b$ -, and  $c$ -axis for the crystal axes [100], [010], [001], respectively, and  $a$ -cut,  $b$ -cut and  $c$ -cut for the (100), (010), (001) surface cuts, respectively. The coordinate system  $x$ ,  $y$ ,  $z$  will be used to describe the ellipsometry setup and the orientation of the crystal surface with respect to the plane of incidence of the incoming and reflected phonon beam, as shown in Fig. 1b.

The ellipsometry experiments have been performed on

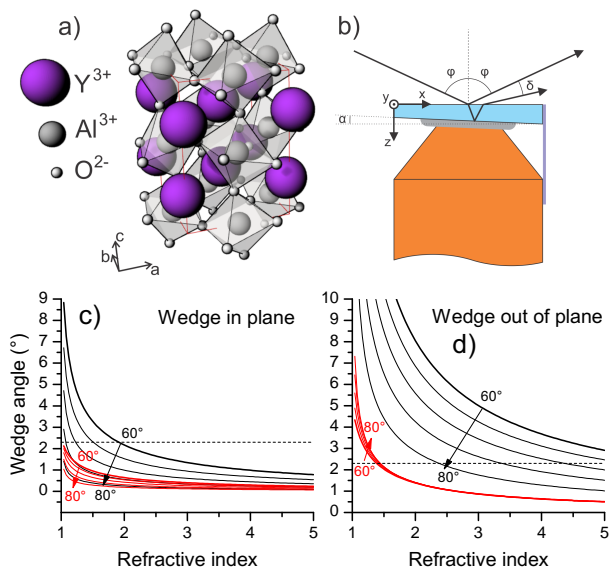


FIG. 1. a) Sketch of the distorted perovskite structure of YAlO<sub>3</sub> with the unit cell indicated by the red lines and the atomic position adapted from [7]. b) Sketch of a YAlO<sub>3</sub> crystal (light blue) with a wedge angle,  $\alpha$ , that is mounted with silver paint (gray) on a copper sample holder (orange). Also shown is the coordinate system of the ellipsometer with the plane of incidence of the photon beam defined by the  $x$ - and  $z$ -axes and the incident and reflected beam at the angle  $\varphi$  with respect to the surface normal. The beam reflected from the backside is deviated by the angle  $\delta$ . The side of the sample is covered by aluminium tape (violet) to further reduce scattered and unwanted light. c) Wedge angle along the plane of incidence that is required for a deviation of  $\delta = 5^\circ$  (red lines) or for a total internal reflection (black lines) calculated as a function of the refractive index and the incidence angle  $\varphi$  ranging from  $60^\circ$  (thick lines) to  $80^\circ$  (indicated by the arrows). d) Same as (c) but with the crystal rotated by  $90^\circ$ , i.e. with the wedge perpendicular to the plane of incidence. Horizontal dashed lines mark a wedge angle of  $2.3^\circ$ .

a set of YAlO<sub>3</sub> crystals with high symmetry surface cuts along (100), (010), and (001) that have been purchased from a commercial vendor (SurfaceNet). For the FIR to UV ranges we used crystals with dimensions of  $5 \times 5 \times 0.5 \text{ mm}^3$ , in the THz range we used two additional, larger crystals with  $10 \times 10 \times 0.5 \text{ mm}^3$ .

The  $5 \times 5 \times 0.5 \text{ mm}^3$  samples have been wedged by mechanical polishing the backside surface such that it is inclined by an angle of  $\alpha = 2.3^\circ$  with respect to front surface (see Fig. 1b). The wedge has been orientated for the  $a$ -cut sample in the  $ab$ -plane; for the  $b$ -cut sample in  $bc$ -plane; and for the  $c$ -cut sample in the  $ca$ -plane. This wedging causes a deviation between the primary beam that is reflected from the front surface and the one reflected from the back surface by an angle of  $\delta$  (indicated in Fig. 1b). This ensures that the light reflected from the back surface does not reach the detector, in the frequency ranges for which YAlO<sub>3</sub> is fully transparent. Moreover, for a large enough angle of incidence of the photons,  $\varphi$ ,

the beam reflected from the backside cannot even exit the sample, due to the total internal reflection at the front surface. Fig. 1c shows the critical wedge angle for this total internal reflection effect (black lines) and for a deviation of the beam by  $\delta = 5^\circ$  (red lines). The latter value corresponds to the maximal acceptance angle of the focusing mirrors of the infrared ellipsometer.

Note that the wedging also helps to avoid unwanted backside reflection if the sample is rotated by  $90^\circ$  around the  $z$ -axis – which is the case when measuring with the plane of incidence along the other high symmetry axis of the crystal. As shown in Fig. 1d, a much larger wedging angle is required here to completely suppress the backside-reflected beam due to the total internal reflection. This is because the wedge angle lies in a plane perpendicular to the plane of incidence and therefore does not add up to the incidence angle. Nevertheless, as long as the refractive index is large enough, i.e. for  $n \geq 1.5$ , the wedge angle of  $2.3^\circ$  leads to deviation of  $\delta > 5^\circ$  out of the plane of incidence that ensures that the beam from the backside does not reach the detector.

The ellipsometry measurements in the infrared range from about 40 to  $5000 \text{ cm}^{-1}$  have been performed with a home-built setup that is attached to a Bruker 70v FTIR spectrometer and has the infrared beam-path in a rough vacuum of about  $10^{-1} \text{ mbar}$ . A more detailed description of the ellipsometer can be found in [21]. It is equipped with a He-flow cryostat (CryoVac) for measurements at temperatures from 10 to 350 K.

In the far-infrared range from 40 to  $700 \text{ cm}^{-1}$ , we used a Hg arc lamp, a solid Si beam-splitter, and a 1.2 K bolometer (Infrared Laboratories) as detector. The ellipsometric measurements have been performed in rotating analyser mode (RAE) with a fixed polarizer (P) in front of the sample (S) and a rotating analyser (A<sub>R</sub>) after the sample (P-S-A<sub>R</sub> configuration). The polarizers made from a metal wire grid on polyethylene substrate have been purchased from a commercial vendor (Tydex). For some measurements, we also used an optional, static compensator (C) that is based on the total internal reflection in a prism of made from undoped Si (P-C-S-A<sub>R</sub> configuration). Since the raw RAE data can be affected by imperfections of the polarizers, and a polarization sensitivity of the detector, the measured data have been treated with a correction algorithm similar to that described in [22]. The details will be discussed elsewhere, together with the calibration procedure for the offsets of the polarizers and the retarder.

In the mid-infrared range, from about 500 to  $5000 \text{ cm}^{-1}$ , we used a Globar source, a Germanium coated KBr beam-splitter, and a 4.2 K bolometer (Infrared Laboratories) as detector. For the latter, the Winston cone has been replaced with a cold focusing optics as to reduce the polarization sensitivity. The polarizer in front of the sample consisted of a high-quality free standing gold wire grid (InfraSpecs). The polarization state after the reflection from the sample has been analysed with a rotating compensator (C<sub>R</sub>) followed by a

static analyser (P-S-C<sub>R</sub>-A configuration). The rotating compensator is based on the internal reflection in a ZnSe prism that is mounted together with three gold mirrors in a four-bounce configuration that can be rotated without changing the beam path to the detector, similar as in [23]. The static analyzer (typically at A=0) consisted of a tandem of KRS5 based grid polarizers (Specac).

All the far- and mid-infrared data have been collected with a resolution of  $2\text{ cm}^{-1}$  and at an incidence angle of  $\varphi = 75^\circ$ . The mid-infrared RCE and far-infrared RAE spectra have shown a very good overlap such that we could simply merge the data, either at  $585\text{ cm}^{-1}$  or at  $540\text{ cm}^{-1}$ . The upper frequency limit of the far-infrared data was determined by the multi-phonon absorption band of Si (beam-splitter and the optional static compensator) between  $600\text{--}620\text{ cm}^{-1}$ . The lower limit of the MIR data was determined by the phonon absorption in the ZnSe prism which sets in below  $520\text{ cm}^{-1}$ .

The high energy spectra from  $0.5$  to  $6.5\text{ eV}$  ( $4033$  to  $52423\text{ cm}^{-1}$ ), spanning the near-infrared, visible, and UV ranges, have been measured with an IR-extended J. A. Woollam VASE instrument, at four angles of incidence ( $55$ ,  $65$ ,  $75$  and  $85^\circ$ ), with a spectral resolution of  $0.05\text{ eV}$ , in an ambient atmosphere.

The low energy spectra in the THz range from  $0.1$  to  $2.5\text{ THz}$  ( $3$  to  $83\text{ cm}^{-1}$ ) have been obtained with a home-built time-domain THz ellipsometer, as described in [24]. This instrument has been operated in a rotating-analyzer (RAE) mode at an incidence angle of  $\varphi = 75^\circ$ . The phase sensitive time-domain detection technique enables one to determine the ellipsometric angles  $\Psi$  and  $\Delta$ , the latter in the full  $360^\circ$  range without the need of additional compensator. The time-resolved detection scheme also allows one to distinguish between the signals that arise from the reflections on the front surface and the back-side that are delayed in time. Accordingly, the contribution of the latter back-side reflection can be removed by cutting the data above a certain time delay. We have used a time window of  $15.5\text{ ps}$  which results in a spectral resolution of about  $1.5\text{ cm}^{-1}$ . To minimize artefacts that may arise from diffraction effects that become increasingly important towards longer wavelength [25], we have used the larger  $10\times 10\times 0.5\text{ mm}^3$  crystals for the THz ellipsometry measurements.

Corresponding broad-band (THz to UV) spectroscopic ellipsometry experiments using the above described combination of ellipsometers have been previously reported for various thin films on isotropic substrates [24, 26–28] and for anisotropic samples [29, 30].

### III. DATA ANALYSIS

The orthorhombic unit cell of  $\text{YAlO}_3$  (see Fig. 1a) contains 4 formula units with 20 atoms and in total 60 degrees of freedom. From all the possible displacement modes, besides the acoustic, Raman-active or silent ones, 25 modes are reported to be infrared-active [11, 12]. The

orthorhombic symmetry yields a diagonal dielectric tensor  $\varepsilon$  with the principal axes oriented along the  $a$ ,  $b$  and  $c$  lattice directions and 9 modes in the  $\varepsilon_a$  component, 9 modes in  $\varepsilon_b$ , and 7 modes in  $\varepsilon_c$ .

The samples were measured in high symmetry configurations for which the  $x$ ,  $y$ , and  $z$  axes, that define the plane of incidence of the ellipsometer and the measured surface of the  $\text{YAlO}_3$  crystal (see Fig. 1b), coincide with the  $a$ ,  $b$  and  $c$  axes directions of the  $\text{YAlO}_3$  crystals for any of the 6 possible permutations. For these high symmetry configurations the birefringence does not give rise to a mixing of the  $p$ - and  $s$ -components. In the following, we describe the reflection and refraction in the framework of the  $x$ - and  $z$ -components of the wavevectors. For the sake of brevity, we use the geometrical components,  $\kappa$ , that are related to the physical wavevector,  $\mathbf{k}$ , according to  $\mathbf{k} = \kappa\omega/c$ . The incident wavevector (in vacuum) is denoted as  $\kappa_{inc} = (\xi, 0, q)$ , with  $\xi = \sin\varphi$  and  $q = \cos\varphi$ . The  $x$ -component  $\xi$  is conserved for the reflected as well as the refracted beams in  $p$ - and  $s$ -polarization. Accordingly, the reflection problem can be treated as stationary in  $x$  and independent of the  $y$ -component [31]. For the  $z$ -components of the two refracted beams denoted as  $\kappa_p$  and  $\kappa_s$ , it follows that:

$$\kappa_p = \sqrt{\varepsilon_x \left(1 - \frac{\xi^2}{\varepsilon_z}\right)}, \quad \kappa_s = \sqrt{\varepsilon_y - \xi^2}, \quad (1)$$

where  $\varepsilon_x$ ,  $\varepsilon_y$  and  $\varepsilon_z$  are the elements of the diagonal dielectric tensor, i.e. one of the permutations of  $\varepsilon_a$ ,  $\varepsilon_b$  and  $\varepsilon_c$ . The Jones matrix thus acquires a diagonal shape, with the following Fresnel coefficients  $r_p$  and  $r_s$  on the diagonal:

$$r_p = \frac{\kappa_p - \varepsilon_x q}{\kappa_p + \varepsilon_x q}, \quad r_s = \frac{q - \kappa_s}{q + \kappa_s}. \quad (2)$$

Note that we employ Fresnel's convention for  $r_p$  [32].

The ellipsometric response is traditionally written in terms of the complex ratio  $\rho = r_p/r_s = \tan\Psi \exp(i\Delta)$ , with the ellipsometric angles  $\Psi$  and  $\Delta$ . In RAE or RCE mode, the directly accessible quantities are the components of the normalized Muller matrix, which in the high symmetry configuration with diagonal Jones matrices acquires the following block-diagonal form,

$$\hat{M} = \begin{bmatrix} 1 & N & 0 & 0 \\ N & 1 & 0 & 0 \\ 0 & 0 & C & S \\ 0 & 0 & -S & C \end{bmatrix}, \quad (3)$$

The elements of this so-called NCS-form of the Mueller matrix are related to the ellipsometric angles by  $N = -\cos 2\Psi$ ,  $C = \sin 2\Psi \cos \Delta$ , and  $S = \sin 2\Psi \sin \Delta$ . Effects from depolarization are not considered here.

In the simplest case of RAE in P-S-A<sub>R</sub> configuration, with the polarizer set to  $P = 45^\circ$ , the modulation of the intensity at the detector, as a function of the analyzer azimuth  $A$ , is given by  $I(A) = I_0(1 + N \cos 2A + C \sin 2A)$ ,

i.e. the  $N$  and  $C$  components are measured directly. In P-C-S-A<sub>R</sub> configuration, with an ideal  $\lambda/4$ -retarder as a static compensator and  $P = 45^\circ$ , the intensity at the detector follows  $I(A) = I_0(1 + N \cos 2A + S \sin 2A)$ , hence the remaining element  $S$  of the sample NCS Mueller matrix is determined. The far-infrared data presented below have been obtained using this approach.

With a rotating compensator (RCE), in P-S-C<sub>R</sub>-A configuration, as it has been used in the mid-infrared range, the modulation at the detector is

$$I(B) = I_0 \left( 1 + \frac{N}{2+N} \cos 4B + \frac{C}{2+N} \sin 4B - \frac{S}{2+N} \sin 2B \right),$$

where  $B$  is the azimuth of the rotating compensator. Therefore, RCE provides access to all three  $N$ ,  $C$ ,  $S$  elements, with  $P = 45^\circ$  and  $A = 0$ , see e.g. [33].

The detection of amplitude and phase by the time-domain THz spectroscopic technique allows measuring directly the complex ratio  $\rho = \tan \Psi \exp i\Delta$ , [34, 35], or, in a general sense, the components of the complex Jones matrix. To facilitate the comparison with the infrared data, the measured spectra in the THz range are also shown in terms of the Mueller matrix elements  $N$ ,  $C$ ,  $S$ .

The three diagonal elements of dielectric tensor of YAlO<sub>3</sub>,  $\varepsilon_a$ ,  $\varepsilon_b$  and  $\varepsilon_c$ , are calculated in the infrared range with the following harmonic-oscillator approximation (HOA):

$$\varepsilon_j(\omega) = \varepsilon_{\infty j} + \sum_{i=1}^{N_j} \frac{A_{ji} \omega_{\text{TO}ji}^2}{\omega_{\text{TO}ji}^2 - \omega^2 - i\omega\gamma_{ji}}, \quad (4)$$

where  $j = a, b, c$ ;  $\varepsilon_{\infty j}$  is the high-frequency dielectric constant,  $N_j = 9$  for  $j = a, b$  and  $N_j = 7$  for  $j = c$ . The parameters  $A_{ji}$ ,  $\omega_{\text{TO}ji}$ ,  $\gamma_{ji}$  account for the strength  $A = \Delta\varepsilon(\omega = 0)$ , the transversal optical resonance frequency  $\omega_{\text{TO}}$ , and the broadening  $\gamma$  of the individual oscillators. The corresponding longitudinal optical phonon frequencies,  $\omega_{\text{LO}ji}$ , coincide with the poles of  $1/\varepsilon_j(\omega)$  in the limit  $\gamma_{ji} \rightarrow 0$ . From this dielectric tensor, the  $z$ -components of  $\kappa_p$  and  $\kappa_s$  (Eq.(1)) have been calculated, for a given angle of incidence,  $\varphi$ , and the particular high symmetry orientation. Subsequently, the Fresnel coefficients (Eq.(2)), their ratio  $\rho$ , and finally the Mueller matrix elements have been derived and fitted to the experimental NCS data, by varying the parameters of the phonon oscillator parameters in Eq.(4).

As a curiosity, we also discuss how the negative refraction effects, which can occur in the vicinity of the longitudinal optical phonon modes ( $\omega_{\text{LO}}$ ) of such anisotropic crystals, show up in the ellipsometric spectra. According to the original work of Veselago [36], a negative refractive index can occur if both the real parts of the permittivity  $\varepsilon$  and the permeability  $\mu$  are negative. Of the two solutions of the complex square-root,  $N = n + ik = \sqrt{\varepsilon\mu}$ , the physically relevant one requires  $k > 0$  and thus  $n < 0$ , such that the plane waves propagate in a direction that

is opposite to the one of the energy flow (or the Poynting vector). This is equivalent to the statement that whenever the product of generally complex values of  $\varepsilon$  and  $\mu$  acquires a negative imaginary part, the physically correct solution of the square root is the one with positive imaginary part ( $k > 0$ ), eventually leading to  $n < 0$  [37].

A similar situation can appear in the expression of the  $p$ -polarized reflection from an anisotropic material. The expression for  $\kappa_p$  in Eq. (1) reveals that negative refraction can occur if the real parts of the dielectric function fulfil the condition that  $\varepsilon_x > 0$  and  $\varepsilon_z < 0$  [38]. This occurs naturally in an anisotropic material in the vicinity of  $\omega_{\text{LO}}$ . However, this is complicated by the fact that  $\varepsilon_x > 0$ ,  $\varepsilon_z < 0$  will lead to negative refraction in terms of Poynting vector  $\mathbf{S}$ , but positive (forward-wave) solution for  $\kappa_p$ . Vice versa, negative  $\kappa_p$ , characterized by backward wave propagation (negative refractive index), will lead to “positive” refraction in terms of energy flow, when the condition is reversed,  $\varepsilon_x < 0$ ,  $\varepsilon_z > 0$  [39].

Indeed, such a negative refraction effect has been observed for several crystals, e.g. Quartz [40] or MgF<sub>2</sub> [41] and it appears also in the anisotropic effective response of dielectric heterostructures [42] and their ellipsometric spectra [43]. We will discuss the corresponding features in the ellipsometric data of the orthorhombic YAlO<sub>3</sub>.

## IV. RESULTS AND DISCUSSION

Figs. 2a, 3a and 4a show the infrared ellipsometry spectra at room temperature measured on the three different high symmetry surfaces for 6 high symmetry configurations. Fig. 2a shows the spectra for the  $b$ -cut and  $c$ -cut surfaces with the  $a$ -axis parallel to the  $x$ -axis (plane of incidence) of the ellipsometer ( $abc, acb \leftrightarrow xyz$ ). Fig. 3a displays the corresponding spectra with the  $b$ -axis parallel to  $x$  for the  $a$ -cut and  $c$ -cut surfaces ( $bac, bca \leftrightarrow xyz$ ) and Fig. 4a with the  $c$ -axis axis parallel to  $x$  for  $a$ -cut and  $b$ -cut surfaces ( $cab, cba \leftrightarrow xyz$ ).

### A. Pseudo-isotropic response

In addition to the measured spectra (coloured symbols), Figs. 2a, 3a and 4a also show the best fits with the anisotropic model (coloured lines) and, for comparison, the simulated ellipsometric spectra (using the fit parameters derived with the anisotropic model) for the fictive scenario of an isotropic response for  $\varepsilon_a$ ,  $\varepsilon_b$ , and  $\varepsilon_c$ , respectively (grey lines). These isotropic spectra serve to highlight spectral ranges where the anisotropy has a clear effect on the experimental data. They make it apparent that in large parts the ellipsometric data are dominated by the dielectric tensor component along the axis  $x$  direction. This circumstance is also evident from Eq. (2), where  $r_p$  depends explicitly on  $\varepsilon_x$ , due to the matching condition of the in-plane components of the electromagnetic field on the interface. Moreover, in Eq. (1) the

value of  $\varepsilon_z$  appears only in the denominator of  $r_p$  such that  $\kappa_p \approx \sqrt{\varepsilon_x}$  if  $\varepsilon_z \gg 1$ .

Nevertheless, the measured far infrared spectra also reveal some clear deviations from the isotropic model that occur in the vicinity of the LO frequencies of the response functions in the  $y$  and  $z$  directions (marked by vertical dashed lines). These anisotropy features will be discussed further below. At first, we discuss the pseudo-isotropic behaviour of the NCS spectra. The frequencies of the TO and LO phonon modes in the spectra of  $\varepsilon_a$ ,  $\varepsilon_b$ , and  $\varepsilon_c$  (as fitted with the anisotropic model) are marked by black and grey arrows in the bottom panels of Figs. 2a, 3a and 4a, respectively. Note that our definition of  $N = -\cos 2\Psi$  differs in sign with respect to the convention used in most textbooks ( $N = \cos 2\Psi$ ). This sign change has the advantage that i) the value of  $N$  equals the Mueller matrix element  $N = m_{21} = m_{12}$ , ii) the shape of the  $N$ -spectra resembles that of  $\Psi$ , or  $\tan \Psi$  (which is widely used for presenting ellipsometric data) and iii) their shape is also reminiscent of the normal incidence reflectivity,  $R$ . Accordingly, the so-called Reststrahlen bands are clearly visible in the spectra of  $N$  as maxima that span the region of the TO-LO splitting of the phonon modes, at which  $N \rightarrow 0$  (or  $\Psi \rightarrow 45^\circ$  and  $R \rightarrow 1$ ). The Mueller matrix element  $S$  is complementary to  $N$ , since its value approaches zero ( $S \rightarrow 0$ ) between the Reststrahlen bands, that is, for range between LO and the following TO frequency. The Mueller matrix element  $C$  has a characteristic zigzag shape with maxima at the TO and minima at the LO frequencies. From there it can be inferred that ellipsometric data in NCS form are equally well represented by the dielectric function  $\varepsilon$  as they are by its inverse  $1/\varepsilon$ , suggesting the use of the factorized dielectric function, as introduced by Gervais and Piriou [44] and discussed in the context of ellipsometry by Schubert et al. [15] and references therein. However, we do not see any indication of asymmetric phonon line-shapes (different broadening of the LO and TO modes) and we parameterized the dielectric functions with harmonic oscillator approximation as in Eq.(4). Indications of a slightly enhanced broadening have only been observed at the highest LO edge and will be discussed further below.

Towards very low frequencies in the THz regime, the measured spectra start to exhibit significant deviations from those of the model curves that are caused by diffraction effects [25]. In particular, the spectra of  $S$  exhibit a steep downturn below approximately  $100 \text{ cm}^{-1}$ . The spectra of  $N$  and  $C$  are less strongly affected by the diffraction and show clear deviations only below  $20 \text{ cm}^{-1}$ . Besides these diffraction artefacts (which prevail below  $100 \text{ cm}^{-1}$ ), the  $a$ -cut  $b$ -axis data of the element  $S$ , in Fig. 3a, are slightly deviating from the expected model values below  $250 \text{ cm}^{-1}$ . Likely, this experimental artefact is caused by a backside reflection or light that is otherwise scattered (but still reaches the detector). Otherwise, the model curves show excellent agreement with the measured data and thus allows us to identify and interpret

the observed features.

## B. Anisotropy features

With the help of the above-described model, we can now discuss the signatures of the anisotropy in the ellipsometry spectra of Fig. 2 to 4. These are marked by the vertical dashed lines across the NCS panels in Figs. 2a, 3a, and 4a. They highlight that the anisotropy effects generally occur in the vicinity of the LO modes of those crystal axes that are oriented along the  $y$ - and  $z$ -direction of the coordinate system of the ellipsometer (see Fig. 1b). Note that only those LO modes have been marked that lead to the strongest anisotropy effects in the data.

Up to approximately  $600 \text{ cm}^{-1}$  the spectra follow mostly the isotropic model, the anisotropy only gives to some rather weak and localized features near the LO frequencies. This changes above  $600 \text{ cm}^{-1}$  where the spectra reveal strong anisotropy features, in particular, in the ranges from  $600$  to  $650 \text{ cm}^{-1}$  and from  $800$  to  $900 \text{ cm}^{-1}$ . The response in the range from  $600$  to  $650 \text{ cm}^{-1}$  is somewhat complicated by the overlap of the TO and LO modes from all three directions, with relatively strong LO modes but rather broad and thus weak TO modes that are superimposed on a weak dielectric background. Notably, the strong anisotropy features around  $850 \text{ cm}^{-1}$  appear well above the highest LO frequencies that are similar for all three axes and occur at  $750$ - $770 \text{ cm}^{-1}$  (see Fig. 4e, inset in the middle panel of Fig. 4a). Such features, above the highest LO frequency, are commonly observed in the ellipsometric spectra of orthorhombic and tetragonal systems [15, 16]. They occur at the end of the Reststrahlen band, which in normal-incidence reflectivity experiment coincides with  $\omega_{\text{LO}}$  (where  $\varepsilon \leftarrow 0$ ), but for an oblique angle of incidence,  $\varphi$ , is shifted to the frequency at which  $\varepsilon \sim \sin^2 \varphi$ , i. e. to the point where the  $z$ -component of the wavevector vanishes (see Eq. (1)). In the literature this frequency is commonly denoted as  $\omega_{\text{LO}^*}$ . The shift of the Reststrahlen band edge with the angle of incidence occurs also for isotropic materials, but without the anisotropy effects.

The strong features that occur around the  $\omega_{\text{LO}^*}$  point in the response of anisotropic samples arise from the difference between the  $\omega_{\text{LO}^*}$  frequencies of the dielectric tensor components that are aligned with the  $x$ ,  $y$ , and  $z$  directions. Specifically, the strong peaks and dips appear around the frequencies at which the dielectric functions  $\varepsilon_a$ ,  $\varepsilon_b$  or  $\varepsilon_c$  are crossing the value of  $\sin^2 \varphi$  ( $\equiv \xi^2$  in Eq. (1)). For the presented data, which have been obtained for an angle of incidence  $\varphi = 75^\circ$ , this corresponds to the condition  $\sin^2 \varphi = 0.933$  that has been marked with a horizontal line in Fig. 4e and yields estimates of  $\omega_{a,\text{LO}^*} \approx 834 \text{ cm}^{-1}$ ,  $\omega_{b,\text{LO}^*} \approx 829 \text{ cm}^{-1}$ , and  $\omega_{c,\text{LO}^*} \approx 841 \text{ cm}^{-1}$ . Also marked are the frequencies at which the dielectric functions reach unity and thus equal that of the ambient. This matching with the dielectric constant of the ambient occurs at  $842 \text{ cm}^{-1}$ ,  $836 \text{ cm}^{-1}$

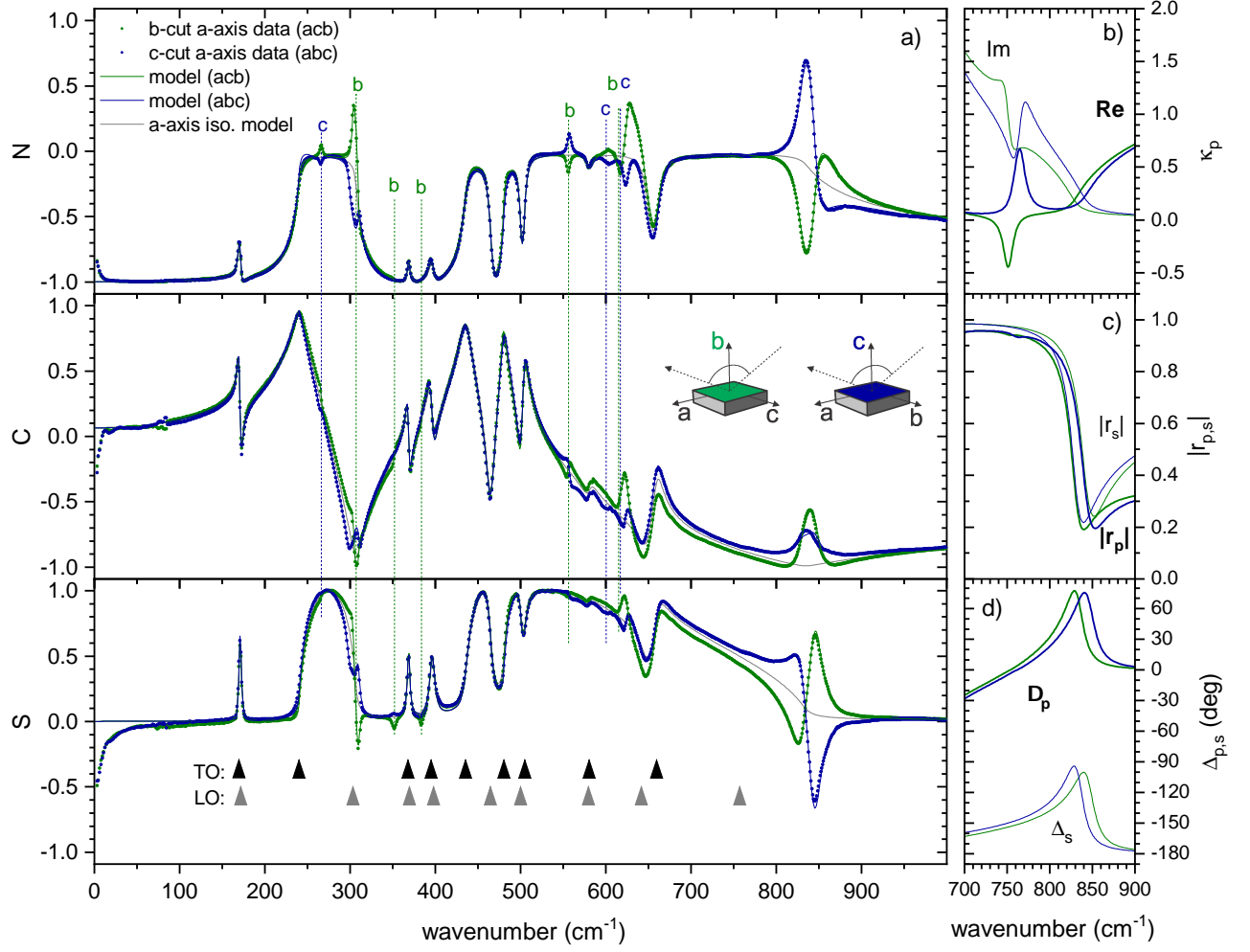


FIG. 2. a) Far-infrared ellipsometry spectra of the Mueller matrix elements  $N$ ,  $C$ ,  $S$  of  $\text{YAlO}_3$  at 300 K with angle of incidence  $\varphi = 75^\circ$  measured on  $b$ -cut (green points) and  $c$ -cut (blue points) surfaces with the  $a$ -axis parallel to the plane of incidence. Sketches of the measurement configurations are shown in the inset of the middle panel. Also shown are the best fits with the anisotropic model (blue and green lines) and, for comparison, the spectra for a fictive sample with an isotropic response that have been calculated with the parameters of  $\varepsilon_a$  (gray lines). Marked by arrows on the bottom panel are the positions of  $\omega_{\text{TO}}$  (black arrows) and  $\omega_{\text{LO}}$  (gray arrows) of  $\varepsilon_a$ . Dashed vertical lines highlight some of the pronounced anisotropy features in the vicinity of  $\omega_{\text{LO}}$  in the  $b$ -axis response (green dashed line) and the  $c$ -axis response (blue dashed line). b) Calculated geometric  $z$ -component of the refracted wavevector for  $p$ -polarized light,  $\text{Re}\{\kappa_p\}$  (thick lines) and  $\text{Im}\{\kappa_p\}$  (thin lines), with the colours matching the configuration of the experiment. c) Calculated absolute values of the Fresnel coefficients  $|r_p|$  (thick lines) and  $|r_s|$  (thin lines). d) Calculated argument of the complex Fresnel coefficients  $\arg(r_p) = \Delta_p$  (thick lines) and  $\arg(r_s) = \Delta_s$  (thin lines).

and  $848 \text{ cm}^{-1}$  for  $\varepsilon_a$ ,  $\varepsilon_b$  and  $\varepsilon_c$ , respectively. At these frequencies, the Fresnel coefficients acquire their extremal values, as well as their ratio  $\rho = r_p/r_s$ , and subsequently  $\Psi$ ,  $\Delta$ , or  $N$ ,  $C$ ,  $S$ . The strong spectral features that originate from the contrast between  $r_p$  and  $r_s$ , are governed here by the divergence of the  $\xi^2/\varepsilon_z$  term in Eq. (1) which strongly impacts  $r_p$  (but not  $r_s$ ). This is unlike the pseudo-isotropic parts of the spectra below  $600 \text{ cm}^{-1}$  for which  $r_p$  is dominated by  $\varepsilon_x$ . Note that in both cases the  $y$ -response solely affects  $r_s$ .

As a result, in the vicinity of  $\omega_{\text{LO}}^*$  it is the contrast between  $\varepsilon_z$  and  $\varepsilon_y$  that gives rise to the anisotropy fea-

tures in the ellipsometry spectra that appear in the same frequency range but show opposite trends (minima versus maxima) for the pairs of different configurations ( $abc$  versus  $acb$  in Fig. 2a,  $bac$  versus  $bca$  in Fig. 3a and  $cab$  versus  $cba$  in Fig. 4a). Note that this mutually opposite behaviour is a general characteristic for all the anisotropy features of the infrared spectra.

This effect can be understood as follows: Fig. 2b displays the  $z$ -component of the geometrical wave-vector of the  $p$ -polarized light,  $\kappa_p$ , for the two configurations  $abc$  and  $acb$ , calculated using the values of the best fit with the anisotropic model. For the moment we skip the fea-

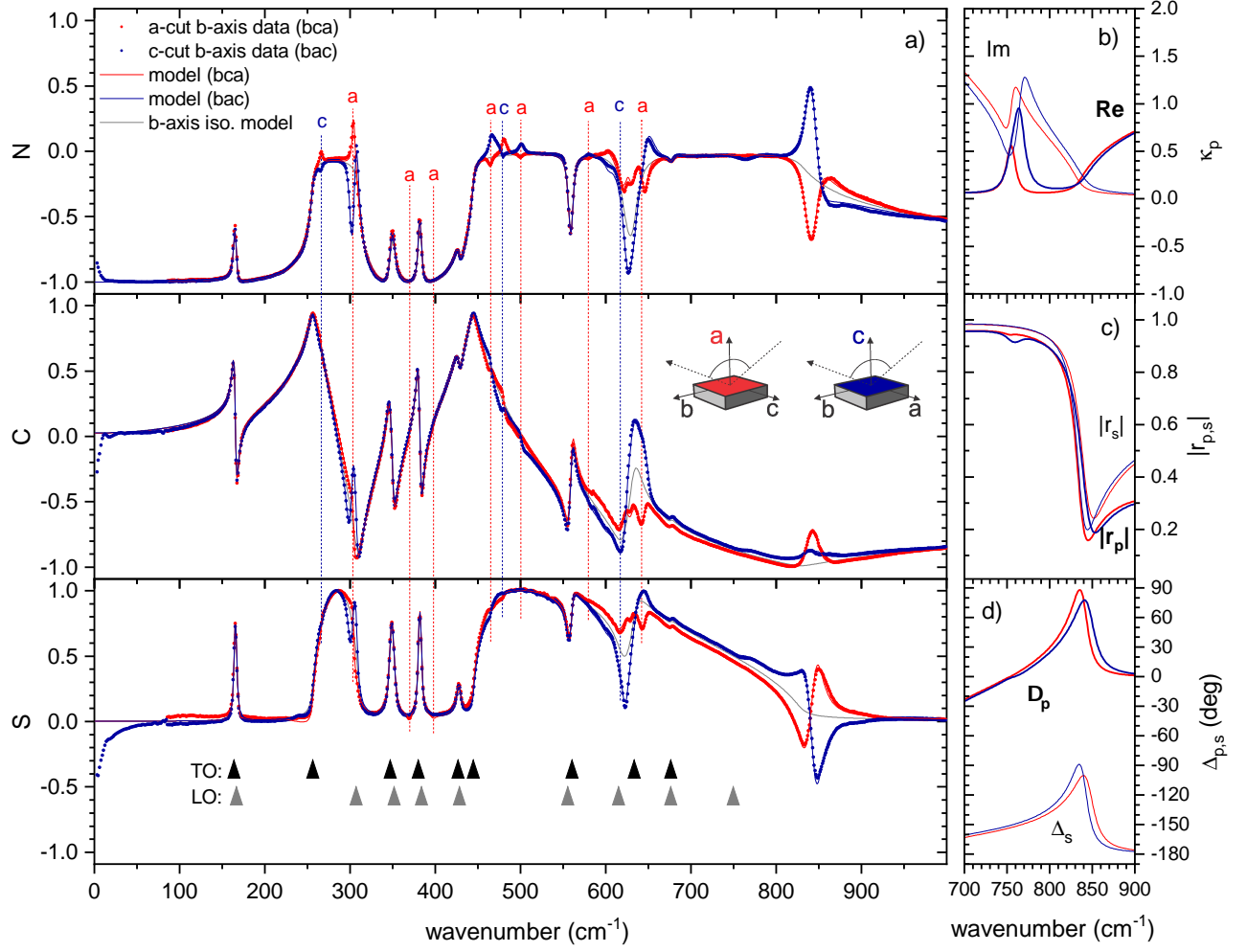


FIG. 3. a) Far-infrared response along the  $b$ -axis of  $\text{YAIO}_3$  at 300 K with  $\varphi = 75^\circ$  measured on  $a$ -cut (red points) and  $c$ -cut (blue points) surfaces (see the sketches in the inset of the middle panel) and expressed in terms of the Mueller matrix elements  $N$ ,  $C$ ,  $S$ . Also shown are the best fits with the anisotropic model (red and blue lines) as well as the simulated response of a fictive isotropic sample with the  $\varepsilon_b$  parameters as obtained from the anisotropic model (gray lines). Arrows on the bottom panel mark the positions of  $\omega_{\text{TO}}$  (black arrows) and  $\omega_{\text{LO}}$  (gray arrows) of  $\varepsilon_b$ . Dashed vertical lines highlight some of the pronounced anisotropy features in the vicinity of  $\omega_{\text{LO}}$  in the  $a$ -axis response (red dashed line) and the  $c$ -axis response (blue dashed line). b) Calculated geometric  $z$ -component of the refracted wavevector for  $p$ -polarized light,  $\text{Re}\{\kappa_p\}$  (thick lines) and  $\text{Im}\{\kappa_p\}$  (thin lines), with colours matching the configuration of the experiment. c) Calculated absolute values of the Fresnel coefficients  $|r_p|$  (thick lines) and  $|r_s|$  (thin lines). d) Calculated argument of the complex Fresnel coefficients  $\arg(r_p) = \Delta_p$  (thick lines) and  $\arg(r_s) = \Delta_s$  (thin lines).

ture occurring at the actual  $\omega_{\text{LO}}$ , which will be discussed later. In general, the position of  $\omega_{\text{LO}^*}$  coincides with the minimum of the absolute value of  $\kappa_p$ . For the  $b$ -cut surface ( $b \parallel z$ ) the minimum of  $|\kappa_p|$  thus occurs at  $\omega_{b,\text{LO}^*}$  and for the  $c$ -cut sample ( $c \parallel z$ ) at  $\omega_{c,\text{LO}^*}$ . The corresponding  $s$ -component,  $\kappa_s$  (not plotted), has an overall similar shape with a minimum at the  $\omega_{\text{LO}^*}$  of the  $y$ -axis response, but does not contain the features related to  $\omega_{\text{LO}}$ . The magnitudes of the corresponding complex Fresnel coefficients  $|r_p|$  and  $|r_s|$  are plotted in Fig. 2c, and their phases  $\Delta_p$  and  $\Delta_s$  on Fig. 2d.

The minima of  $|\kappa_{s,p}|$  at  $\omega_{\text{LO}^*}$  also give rise to characteristic features in spectra phase shifts,  $\Delta_p$  and  $\Delta_s$ . For

the  $b$ -cut surface,  $\Delta_p$  and  $\Delta_s$  have fairly sharp maximum at  $\omega_{b,\text{LO}^*} = 829 \text{ cm}^{-1}$  and  $\omega_{c,\text{LO}^*} = 841 \text{ cm}^{-1}$ , respectively. For the  $c$ -cut surface, this order is inverted, i.e. the maxima of  $\Delta_p$  and  $\Delta_s$  occur at  $\omega_{c,\text{LO}^*} = 841 \text{ cm}^{-1}$  and  $\omega_{b,\text{LO}^*} = 829 \text{ cm}^{-1}$ , respectively. These splitting of the maxima of the phase shifts  $\Delta_p$  and  $\Delta_s$ , for which the order is inverted between  $b$ - and  $c$ -cut surfaces, gives rise to pronounced features (dips and kinks) in the ellipsometric angle Delta ( $\Delta = \Delta_p - \Delta_s$ ), and consequently in the Mueller matrix element  $S$  in the lower panel of Fig. 2a. For the latter, the extrema are slightly shifted, i.e. they occur slightly below  $\omega_{b,\text{LO}^*} = 829 \text{ cm}^{-1}$  and slightly above  $\omega_{c,\text{LO}^*} = 841 \text{ cm}^{-1}$ .

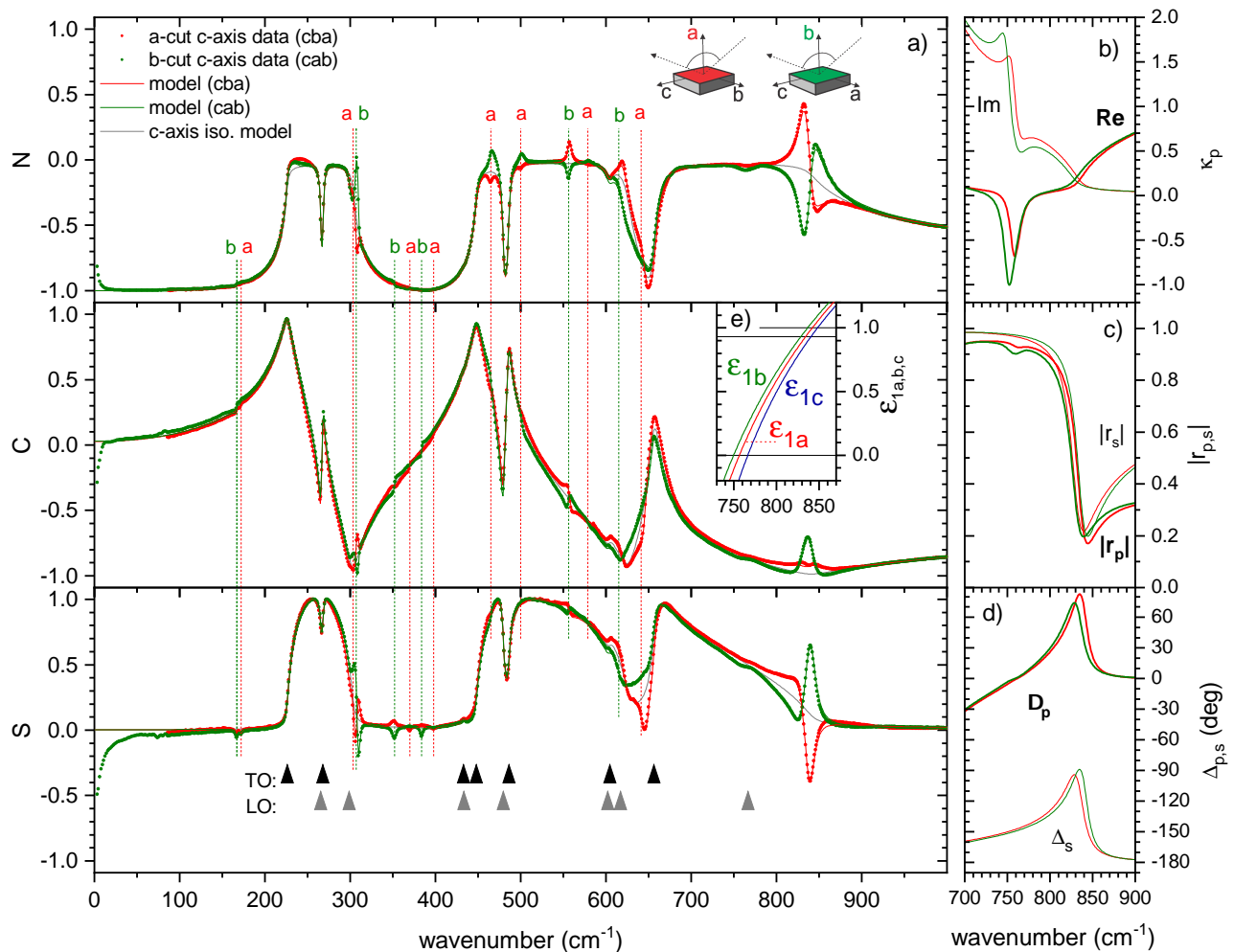


FIG. 4. a) Far-infrared response along the  $c$ -axis of  $\text{YAIO}_3$  at 300 K with  $\varphi = 75^\circ$  as measured on  $a$ -cut (red points) and  $b$ -cut (green points) surfaces and shown by the Mueller matrix elements  $N$ ,  $C$ ,  $S$ . Also displayed are the best fits with the anisotropic model (red and green lines) and the response of a fictive isotropic sample simulated with the  $\varepsilon_c$  parameters (gray lines). The inset of the middle panel shows a comparison of the modelled spectra of the real part of dielectric functions  $\varepsilon_a$ ,  $\varepsilon_b$ , and  $\varepsilon_c$ . Arrows on the bottom panel mark the positions of  $\omega_{\text{TO}}$  (black arrows) and  $\omega_{\text{LO}}$  (gray arrows) of  $\varepsilon_c$ . Dashed vertical lines highlight some of the pronounced anisotropy features in the vicinity of  $\omega_{\text{LO}}$  in the  $a$ -axis response (red dashed line) and the  $b$ -axis response (green dashed line). b) Calculated geometric  $z$ -component of the refracted wavevector for  $p$ -polarized light,  $\text{Re}\{\kappa_p\}$  (thick lines) and  $\text{Im}\{\kappa_p\}$  (thin lines), with colours matching the configuration of the experiment. c) Calculated absolute values of the Fresnel coefficients  $|r_p|$  (thick lines) and  $|r_s|$  (thin lines). d) Calculated argument of the complex Fresnel coefficients  $\arg(r_p) = \Delta_p$  (thick lines) and  $\arg(r_s) = \Delta_s$  (thin lines).

For the interpretation of the corresponding feature in  $N$ , we recall that  $N$  is closely related to the ellipsometric angle  $\Psi$  ( $N = -\cos 2\Psi$ ), and  $\tan \Psi = |r_p|/|r_s|$ . The extremum in  $N$  coincides here with the minima of  $|r_p|$  and  $|r_s|$  (Fig. 2c) which occur at the point at which the contrast between dielectric constant of the sample and the ambient vanishes. For  $|r_s|$  this occurs as the  $y$ -axis response crosses unity, i.e. for the  $c$ -cut surface ( $abc$ ) at  $836 \text{ cm}^{-1}$  for  $\varepsilon_b$  and for the  $b$ -cut surface ( $acb$ ) at  $848 \text{ cm}^{-1}$  for  $\varepsilon_c$ . Note that a finite absorption broadens these  $|r_s|$  minima and shifts them to slightly higher frequencies.

The coefficient  $|r_p|$  depends in general on both the  $x$ -

axis and  $z$ -axis responses (see Eq. 1, 2). However, since in the relevant range both of them are close to unity, the minimum of  $|r_p|$  is more sensitive to the  $z$ -axis response and appears slightly above the point where the  $z$ -axis response crosses unity. Note that this  $|r_p|$  minimum also represents one of the solutions for the general Brewster condition [38].

For the sake of completeness, we have also plotted the corresponding  $\kappa_p$ ,  $|r_p|$  and  $|r_s|$  spectra for the other sample orientations and measurement configurations in Fig. 3b-d and 4b-d. The resulting anisotropy effects in the NCS spectra are analogous to the ones that we have discussed above for the  $abc$  and  $acb$  configurations that are

displayed in Fig. 2a. They simply involve different permutations of the  $a$ -,  $b$ - or  $c$ -components of the relevant critical frequencies.

The above discussion about the large anisotropy features in the ellipsometric response in the range from 800 to 900  $\text{cm}^{-1}$  can be summarized as follows: The features in the Mueller matrix element  $N$  (or in the ellipsometric angle  $\Psi$ ) are related to the anisotropy of the minima in  $|r_p|$  and  $|r_s|$  that occur if the dielectric function of the sample matches that of the ambient (i.e.  $\varepsilon \rightarrow 1$  in case of vacuum ambient). The corresponding features in the Mueller matrix element  $S$  (or in  $\Delta$ ) depend on the actual anisotropy of  $\omega_{\text{LO}^*}$  ( $|\kappa| \rightarrow 0$ , onset of total reflection), which at  $\varphi = 75^\circ$  yields the condition  $\varepsilon = 0.933$ . Note that both kind of features get broadened and slightly shifted by the nonzero imaginary parts of the response functions. Moreover, since these critical points tend to be rather close in frequency, the different contributions to the anisotropy effects in NCS are partially merged, especially if the angle of incidence is large with  $\xi^2 \rightarrow 1$ . Measurements at a lower angle of incidence would allow one to better separate the features appearing at  $\omega_{\text{LO}^*}$  and at  $\varepsilon \rightarrow 1$ . In both cases, however, these anisotropy features are directly related to the differences of the  $z$ -axis and  $y$ -axis response functions ( $\varepsilon_z$  and  $\varepsilon_y$ ). Notably, near  $\omega_{\text{LO}^*}$  these features are almost independent of  $\varepsilon_x$  – although at lower frequencies, the  $x$ -axis response dominates the ellipsometry spectra.

Note that the smaller anisotropy effects that appear near the  $\omega_{\text{LO}}$  frequencies in the range below 600  $\text{cm}^{-1}$  (marked by the vertical dashed lines in Figs. 2a, 3a, 4a) have the same origin as described above for the 800 to 900  $\text{cm}^{-1}$  range. The main difference concerns the separation between  $\omega_{\text{LO}}$ ,  $\omega_{\text{LO}^*}$  and the point of  $\varepsilon \rightarrow 1$  that becomes much smaller.

### C. Negative refraction

Another interesting feature concerns an anomaly in the geometrical  $z$ -component of the refracted wave-vector of the p-polarized beam,  $\kappa_p$ , that occurs in the vicinity of the highest LO mode, i.e. near the zero crossing of the real part of  $\varepsilon$  around 750  $\text{cm}^{-1}$  (see Figs. 2b, 3b and 4b, see also inset Fig. 4e). In the experimental data, the anisotropy of this highest LO mode with  $\omega_{b,\text{LO}} < \omega_{a,\text{LO}} < \omega_{c,\text{LO}}$  gives rise to a small drop in  $N$  (or  $\Psi$ ) and corresponding feature in  $C$  and  $S$ .

Notably, this feature appears well below  $\omega_{\text{LO}^*}$  and thus within the Reststrahlen band, for which in case of an isotropic sample only an evanescent wave (but not a refracted wave) could exist. Such a refracted wave is however possible for the anisotropic case of  $\text{YAlO}_3$  for which the expression for  $\kappa_p$  in Eq. (1) has a non-evanescent solution in the range where  $\varepsilon_x$  and  $\varepsilon_z$  have opposite signs. For the condition  $\varepsilon_x < 0$ ,  $\varepsilon_z > 0$ , there exists a strongly attenuated, but propagating wave that has an unconventional refraction. The real part of the  $z$ -component of

the wave vector  $\kappa_p$ , which determines the direction of the phase propagation, has a negative value such that it describes a backward travelling wave (the  $x$ -component,  $\xi$ , of the wave vector remains positive). Nevertheless, for the energy flow the refraction remains positive since the  $x$ - and the  $z$ -components of the Poynting vector are positive.

For the opposite case of  $\varepsilon_x > 0$  and  $\varepsilon_z < 0$ , there is negative refraction effect: the  $x$ -component of the Poynting vector becomes negative, although the real part of  $\kappa_p$  is positive and the waves are travelling forward from the interface to the bulk [39]. The Figs. 2b, 3b, 4b show the  $\kappa_p$  spectra calculated with the parameters of the best-fit model. In Fig. 2b, the solution for the  $abc$ -configuration has a positive  $\text{Re}\{\kappa_p\}$  around 770  $\text{cm}^{-1}$  – leading to a forward wave but a negative energy refraction. The  $acb$ -configuration shows a negative  $\text{Re}\{\kappa_p\}$  around 750  $\text{cm}^{-1}$  – corresponding to a backward wave with positive energy flow. In Fig. 3b, the  $bac$ - and  $bca$ -configurations have positive  $\text{Re}\{\kappa_p\}$  and negative refraction. Finally, in Fig. 4b, both the  $cab$ - and  $cba$ -configurations have negative  $\text{Re}\{\kappa_p\}$  and positive refraction in the discussed spectral range.

The above discussion raises the question whether based on the ellipsometric data one can tell the difference between the cases of negative and positive refraction. The answer is that the ellipsometry data do not allow on to distinguish between these two cases. Indeed, it turns out that the change in the sign of the real part of  $\kappa_p$  does not give rise to any characteristic feature in  $r_p$  and the resulting Mueller matrix elements  $N$ ,  $C$ ,  $S$  that could serve as indicator. This evident from the comparison of the real part of the  $\kappa_p$  curve for the  $bac$  configuration in Fig. 3b (with positive values) with that of the  $cab$ -configuration in Fig. 4b (with negative values) and an inspection of the resulting NCS spectra in Figs 3a and 4b which exhibit no characteristic difference in the vicinity of the high  $\omega_{\text{LO}}$ .

### D. Dielectric response along the main crystal axes of $\text{YAlO}_3$

Figs. 5a, b and c display the far-infrared dielectric response along the main crystal axes of orthorhombic  $\text{YAlO}_3$  that represent the diagonal elements,  $\varepsilon_a$ ,  $\varepsilon_b$  and  $\varepsilon_c$ , of the dielectric tensor. They have been obtained from a simultaneously fitting with an anisotropic model to the room temperature ellipsometric data for six different configurations of the surface cuts and relative orientations of the crystal axes. The corresponding data and model curves have been presented in Figs. 2a, 3a, and 4a. The model contains a sum of Lorentzian oscillators that describe the response of the infrared active phonons, as given in Eq.(4). With this model, we identified 9 phonons in the  $a$ -axis response,  $\varepsilon_a$ , 9 phonons in the  $b$ -axis response,  $\varepsilon_b$ , and 7 phonons in the  $c$ -axis response,  $\varepsilon_c$ , as predicted from theory [10, 12]. Several of the TO phonons shown in Fig. 5 are rather weak, their position

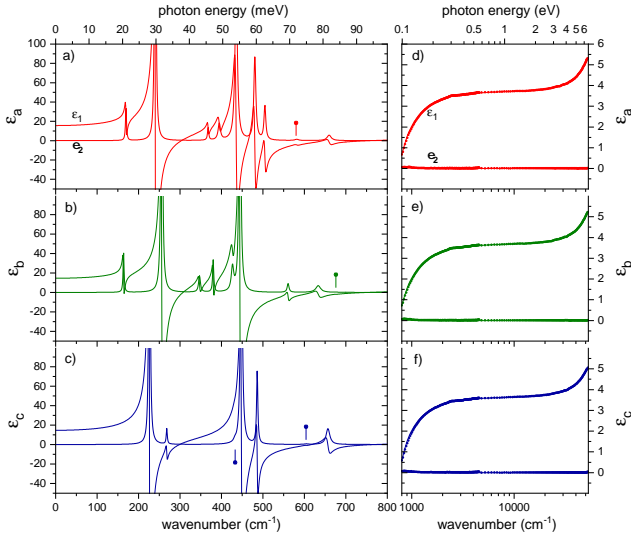


FIG. 5. Diagonal elements of the dielectric tensor along the three main crystal axes of orthorhombic  $\text{YAlO}_3$ . The spectra represent the best fit with an anisotropic model to the ellipsometry data taken at room temperature for six different configurations with respect to the surface cut and the mutual orientation of the crystal axes. Panels a), b), and c) show the far-infrared spectra of  $\varepsilon_a$ ,  $\varepsilon_b$  and  $\varepsilon_c$ , respectively. Thin lines represent the real part of the dielectric function,  $\varepsilon_1$ , thicker lines the imaginary part,  $\varepsilon_2$ . The positions of the weak phonons are marked with the pin symbols. Panels d), e), and f) show the extension of the model in the MIR/NIR/VIS/UV ranges on a logarithmic energy scale. Lines represent an anisotropic Cauchy model. Symbols show the result of an anisotropic point-by-point fit.

has therefore been highlighted with the pin symbols.

The positions,  $\omega_{\text{TO}}$ , broadenings,  $\gamma$ , and oscillator strengths,  $\Delta\varepsilon$ , of the line-shapes were fitting parameters of the model. The obtained best-fit parameters for the room temperature spectra are listed in Table I. The additional fit parameter  $\varepsilon(\infty)$  represents the high-frequency dielectric constant. The LO mode frequencies,  $\omega_{\text{LO}}$ , have been derived from the poles of  $1/\varepsilon$  when  $\gamma \rightarrow 0$ , and  $\varepsilon(0)$  represents the static dielectric constant calculated from the sum of  $\varepsilon(\infty)$  and the oscillator strengths of the phonons,  $\Delta\varepsilon$ .

Except for the highest LO mode, we have found that it is not necessary to introduce an asymmetric broadening, e.g. by using different values for the TO and LO-modes ( $\gamma_{\text{TO}} \neq \gamma_{\text{LO}}$ ) as described by Gervais and Piriou [44]. For practical reasons, we have accounted for the asymmetric broadening of the highest LO mode by introducing instead a nonzero imaginary part of  $\varepsilon(\infty)$ . This additional parameter allowed us to obtain a good fit of the shapes of the anisotropic features at the highest  $\omega_{\text{LO}^*}$ . While such a procedure is somewhat unphysical, since it violates the Kramers-Kronig consistency, we found that it has a negligible impact on the spectra except for the anisotropy features at the highest  $\omega_{\text{LO}^*}$ .

The obtained value of the TO phonon positions listed

in Table I are in rather good agreement with the previous theoretical predictions [10, 12]. Most of the TO eigenfrequencies are within  $3\text{ cm}^{-1}$  of the predicted values. In some cases, the predictions differ up to  $10\text{ cm}^{-1}$  from each other, while the experimental value lies in between. Only in few cases the experimental values differ by up to  $10\text{ cm}^{-1}$  from theory. The phonon at  $432.5\text{ cm}^{-1}$  in the  $c$ -axis response is extremely weak, in the experimental data it is only evident in the  $S$ -element (bottom panel of Fig. 4a), and thus could only be identified with the help of the theory.

Overall, we conclude that  $\text{YAlO}_3$  has very stable and predictable lattice dynamical properties: A single model describes very well the experimental data that have been obtained on three samples with different surface cuts. Moreover, the older and newer theoretical calculations (of TO phonon positions) agree reasonably well and match the data to high accuracy.

Figs. 5d, e and f show the model dielectric functions  $\varepsilon_a$ ,  $\varepsilon_b$  and  $\varepsilon_c$  for an extended energy range that spans the mid-, near-infrared, visible and ultraviolet (up to 6.5 eV). Here, we employed two different modelling approaches. For the first type of fitting, the whole MIR to UV range has been represented by an anisotropic Cauchy dispersion (model lines in Figs. 5d, e, f), while the parameters describing the phonons in the FIR range have been fixed and the FIR data have not been included in the fit. The imaginary part of  $\varepsilon(\infty)$  that was used in the far-infrared fitting has been omitted. These fits have been performed simultaneously on the mid-infrared data, measured in the range 0.1 to 0.5 eV at  $\varphi = 75^\circ$ , and on the NIR-UV data in the range from 0.5 to 6.5 eV measured with a Woollam ellipsometer (VASE) at variable angles of incidence of  $\varphi = 55^\circ, 65^\circ, 75^\circ$  and  $85^\circ$ . As for the phonons in the FIR-range, the fitting has been performed on an extended data set for all the 6 high symmetry configurations.

The surface roughness, which is known to affect especially the data in the VIS/UV region, has been accounted for by introducing an isotropic 50% Bruggeman effective medium (BEMA) layer which mixes the actual  $x$ -axis response of the  $\text{YAlO}_3$  sample (depending on orientation) with the ambient. The obtained thickness values of the BEMA layers are 2.8 nm, 1.9 nm and 4.4 nm for the  $a$ -cut,  $b$ -cut and  $c$ -cut surfaces, respectively.

The best-fit parameters of the Cauchy model are listed in table II. The optimized Cauchy constants  $\varepsilon_{a0}$ ,  $\varepsilon_{b0}$  and  $\varepsilon_{c0}$  differ from the values of  $\varepsilon(\infty)$  listed in Table I. While for an ideal case these parameters should be identical, we could not achieve perfect match of model and data for the entire THz to UV range.

For the second fitting approach, we have fixed the thicknesses of the effective roughness layers, (to the value derived from the Cauchy plus BEMA fit) and fitted the same extended set of ellipsometry data in a point-by-point manner with an unconstrained orthorhombic model (fitting independently the real and imaginary parts of  $\varepsilon_a$ ,  $\varepsilon_b$  and  $\varepsilon_c$ ). The obtained dielectric functions are shown by symbols in Fig. 5d, e and f. It is evident that the result

TABLE I. Infrared model parameters of the anisotropic dielectric response of  $\text{YAlO}_3$  at room temperature.

<i>a</i> -axis				<i>b</i> -axis				<i>c</i> -axis			
$\omega_{\text{TO}}(\text{cm}^{-1})$	$\gamma(\text{cm}^{-1})$	$\Delta\varepsilon$	$\omega_{\text{LO}}(\text{cm}^{-1})$	$\omega_{\text{TO}}(\text{cm}^{-1})$	$\gamma(\text{cm}^{-1})$	$\Delta\varepsilon$	$\omega_{\text{LO}}(\text{cm}^{-1})$	$\omega_{\text{TO}}(\text{cm}^{-1})$	$\gamma(\text{cm}^{-1})$	$\Delta\varepsilon$	$\omega_{\text{LO}}(\text{cm}^{-1})$
169.7	2.9	0.60	171.9	163.8	2.8	0.70	166.8	226.3	3.0	7.12	265.5
240.3	3.0	7.01	303.3	255.9	4.2	5.75	307.1	268.0	2.9	0.17	298.7
367.8	3.5	0.12	369.5	347.0	5.3	0.26	351.6	432.5	6.9	0.04	432.7
394.7	6.7	0.29	397.8	380.0	3.1	0.27	383.7	448.0	5.1	3.08	479.2
435.5	6.7	2.55	464.5	426.6	6.8	0.39	428.3	486.2	3.6	0.56	602.2
480.5	5.7	1.04	500.0	444.5	4.2	3.50	555.6	604.9	11	0.008	616.7
504.7	5.2	0.37	580.2	560.7	5.2	0.08	614.5	656.9	11	0.27	766.5
581.6	10	0.02	642.6	633.5	14	0.15	676.0				
659.7	12	0.10	756.7	676.4	6.9	0.002	749.9				
$\varepsilon(\infty)$	3.58 (+i0.037)			$\varepsilon(\infty)$	3.54 (+i0.048)			$\varepsilon(\infty)$	3.46 (+i0.058)		
$\varepsilon(0)$	15.67			$\varepsilon(0)$	14.65			$\varepsilon(0)$	14.70		

TABLE II. Near-infrared to UV Cauchy model parameters of  $\text{YAlO}_3$ , room temperature. Calculated anisotropic dielectric constant and refractive index at 2 eV.

<i>a</i> -axis		<i>b</i> -axis		<i>c</i> -axis	
$\varepsilon_{a0}$	3.700	$\varepsilon_{b0}$	3.677	$\varepsilon_{c0}$	3.625
$\varepsilon_{a1}$	0.0150 eV <sup>-2</sup>	$\varepsilon_{b1}$	0.0133 eV <sup>-2</sup>	$\varepsilon_{c1}$	0.0142 eV <sup>-2</sup>
$\varepsilon_{a2}$	0.00057 eV <sup>-4</sup>	$\varepsilon_{b2}$	0.00056 eV <sup>-4</sup>	$\varepsilon_{c2}$	0.00048 eV <sup>-4</sup>
$\varepsilon_a(2\text{eV})$	3.764	$\varepsilon_b(2\text{eV})$	3.735	$\varepsilon_c(2\text{eV})$	3.685
$n_a(2\text{eV})$	1.940	$n_b(2\text{eV})$	1.933	$n_c(2\text{eV})$	1.920

of the point by-point fit agrees well with the one derived from the fitting with the parameterized model functions. Notably, no sign of energy gap edge is detected up to 6.5 eV.

### E. Temperature dependence of the phonons $\text{YAlO}_3$

Finally, Fig. 6 shows the temperature dependence of the TO phonon positions between 10 K and 330 K. The full set of fit parameters is available in the supporting information [45]. The temperature dependent measurements were performed on the 3 different surface-cut samples, but in single orientation on each: the *a*-axis response was measured on the *c*-cut sample, the *b*-axis response on the *a*-cut sample and *c*-axis one on the *b*-cut sample. Once the anisotropic model was optimized on the full set of data from 6 orientations at room temperature, the reduced set of 3 orientations has been found to be sufficient to reliably model and fit the temperature dependence of the phonon parameters. Since the temperature dependent measurements have only been performed in the far-infrared part of the spectra below 700 cm<sup>-1</sup>, the highest  $\omega_{\text{LO}}^*$  feature is not included.

As there is no instability or phase transition predicted or observed for  $\text{YAlO}_3$ , the temperature behaviour of the phonon positions is rather conventional. Only the high frequency modes, likely related to oxygen octahedra stretching, show some anomalous temperature dependence. Discussion about origin of the anomalies is

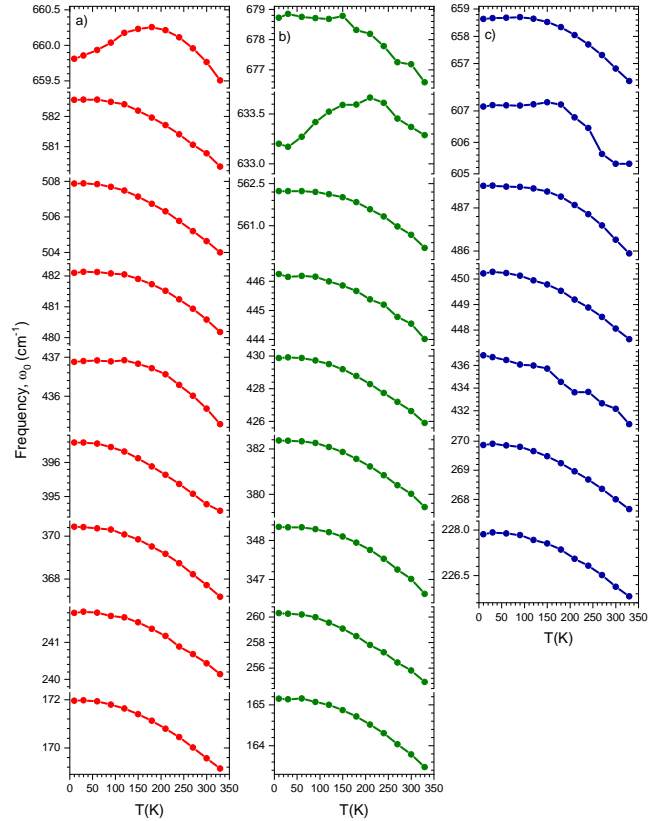


FIG. 6. Temperature dependence of the eigenfrequency  $\omega_0$  of the infrared-active TO phonons of  $\text{YAlO}_3$ : a) *a*-axis response b) *b*-axis response c) *c*-axis response.

beyond the scope of this work.

## V. SUMMARY AND CONCLUSIONS

We have performed broad-band (THz to UV) spectroscopic ellipsometry experiments to determine the full dielectric tensor of the orthorhombic perovskite  $\text{YAlO}_3$ . This material is widely used as substrates for the thin

film growth of complex oxides. The detailed knowledge of its anisotropic dielectric response function is thus a precondition for a correct analysis of the thin film response.

The ellipsometry measurements have been performed for 6 different orientations of the plane of incidence of the photons and the sample surface with respect to the principal axes of the orthorhombic  $\text{YAlO}_3$  crystal. Wedged crystals have been used to avoid artefacts that can arise from photons that are reflected from the backside surface in the frequency ranges where  $\text{YAlO}_3$  is fully transparent, i.e. below about  $100 \text{ cm}^{-1}$  ( $200 \text{ cm}^{-1}$ ) at room temperature (at low temperature) and well above the range of the multi-phonon excitations, i.e. at  $\omega > 1500 \text{ cm}^{-1}$ .

The measured spectra are presented in terms of the Mueller matrix elements  $N$ ,  $C$ , and  $S$ . It is shown that their analysis with an anisotropic model provides robust and unambiguous results that capture all the essential spectroscopic features. In particular, it yields all the infrared-active phonon modes with eigenfrequencies (positions) that agree well with previous reports and theoretical predictions. We also discuss the spectral features that arise from the anisotropy of the dielectric response, including a negative refraction effect that occurs in the vicinity of the highest anisotropic LO-mode,  $\omega_{\text{LO}}$ .

From the 6 possible high-symmetry orientations, we

have compared pairs of NCS datasets taken on different crystal surfaces, but with the same crystal axis oriented along the  $x$ -axis of the instrument coordinate system (intersection of the plane of incidence and the sample surface). This comparison revealed a) quasi-isotropic character of the ellipsometric spectra in the ranges away from the LO frequencies – they are dominated by the response function of the crystal axis aligned with the  $x$  coordinate of the ellipsometer, and b) the anisotropic effects, occurring near the  $\omega_{\text{LO}}$  frequencies of the remaining two crystal axes, are mutually opposite when the  $y$ - and  $z$ -axis responses are interchanged.

Last but not least, we have studied the temperature dependence of the phonon parameters. Whereas no anomalous behaviour has been observed, we expect that the detailed knowledge of the temperature dependent optical response of  $\text{YAlO}_3$  will be useful for future studies of various thin films of complex oxides that are grown on  $\text{YAlO}_3$  substrates.

## ACKNOWLEDGMENTS

We acknowledge funding by the Swiss National Science Foundation (SNSF) through projects No. 200020-172611 and 200021-214905.

- 
- [1] K. S. Bagdasarov and A. A. Kaminskii, JETP LETTERS **9**, 303 (1969).
- [2] M. J. Weber, M. Bass, K. Andringa, R. R. Monchamp, and E. Comperchio, Applied Physics Letters **15**, 342 (1969).
- [3] A. A. Kaminskii, O. Lux, J. Hanuza, H. Rhee, H. J. Eichler, H. Yoneda, J. Zhang, D. Tang, and A. Shirakawa, Laser & Photonics Reviews **8**, 904 (2014).
- [4] K. Shimamoto, S. Mukherjee, N. S. Bingham, A. K. Suszka, T. Lippert, C. Niedermayer, and C. W. Schneider, Physical Review B **95**, 184105 (2017).
- [5] L. Vistoli, W. Wang, A. Sander, Q. Zhu, B. Casals, R. Cichelero, A. Barthélémy, S. Fusil, G. Herranz, S. Valencia, R. Abrudan, E. Weschke, K. Nakazawa, H. Kohno, J. Santamaria, W. Wu, V. Garcia, and M. Bibes, Nature Physics **15**, 67 (2018).
- [6] E. Salje, Physica Status Solidi (a) **22**, K117 (1974).
- [7] J. Suda, O. Kamishima, K. Hamaoka, I. Matsubara, T. Hattori, and T. Sato, Journal of the Physical Society of Japan **72**, 1418 (2003).
- [8] A. Chopelas, Physics and Chemistry of Minerals **38**, 709 (2011).
- [9] M. A. Hernández-Rodríguez, V. Monteseuro, A. D. Lozano-Gorrín, F. J. Manjón, J. González-Platas, P. Rodríguez-Hernández, A. Muñoz, V. Lavín, I. R. Martín, and U. R. Rodríguez-Mendoza, The Journal of Physical Chemistry C **121**, 15353 (2017).
- [10] W. Dewo, K. Łuczyńska, Y. Zorenko, V. Gorbenko, K. Druzbicki, and T. Runka, Spectrochimica Acta Part A: Molecular and Biomolecular Spectroscopy **231**, 118111 (2020).
- [11] H. Gupta and P. Ashdhir, Journal of Solid State Chemistry **146**, 287 (1999).
- [12] R. Vali, Journal of Luminescence **127**, 727 (2007).
- [13] M. Schubert, *Infrared Ellipsometry on Semiconductor Layer Structures* (Springer, 2005) p. 193.
- [14] J. Humlíček, R. Henn, and M. Cardona, Physical Review B **61**, 14554 (2000).
- [15] M. Schubert, T. E. Tiwald, and C. M. Herzinger, Physical Review B **61**, 8187 (2000).
- [16] S. Schöche, T. Hofmann, R. Korlacki, T. E. Tiwald, and M. Schubert, Journal of Applied Physics **113**, 164102 (2013).
- [17] S. Tuménas, P. Mackonis, R. Nedzinskas, L. Trinkler, B. Berzina, V. Korsaks, L. Chang, and M. Chou, Applied Surface Science **421**, 837 (2017).
- [18] A. Mock, R. Korlacki, S. Knight, M. Stokey, A. Fritz, V. Darakchieva, and M. Schubert, Physical Review B **99**, 184302 (2019).
- [19] R. Diehl and G. Brandt, Materials Research Bulletin **10**, 85 (1975).
- [20] Note that the properties can be found on the manufacturer's website. [https://surfacenet.de/files/kristall\\_daten.php?crystal=143](https://surfacenet.de/files/kristall_daten.php?crystal=143).
- [21] C. Bernhard, J. Humlíček, and B. Keimer, Thin Solid Films **455-456**, 143 (2004).
- [22] J. den Boer, G. Kroesen, M. Haverlag, and F. de Hoog, Thin Solid Films **234**, 323 (1993).
- [23] T. N. Stanislavchuk, T. D. Kang, P. D. Rogers, E. C. Standard, R. Basistyy, A. M. Kotelyanskii, G. Nita, T. Zhou, G. L. Carr, M. Kotelyanskii, and A. A. Sirenko, Review of Scientific Instruments **84**, 023901 (2013).

- [24] P. Marsik, K. Sen, J. Khmaladze, M. Yazdi-Rizi, B. P. P. Mallett, and C. Bernhard, *Applied Physics Letters* **108**, 052901 (2016).
- [25] J. Humlíček and C. Bernhard, *Thin Solid Films* **455-456**, 177 (2004).
- [26] B. P. P. Mallett, J. Khmaladze, P. Marsik, E. Perret, A. Cerreta, M. Orlita, N. Biškup, M. Varela, and C. Bernhard, *Physical Review B* **94**, 180503 (2016).
- [27] K. Sen, P. Marsik, S. Das, E. Perret, R. de Andrés Prada, A. Alberca, N. Biškup, M. Varela, and C. Bernhard, *Physical Review B* **95**, 214506 (2017).
- [28] P. Marsik, R. de Andrés Prada, A. Daniil, and C. Bernhard, *Advanced Optical Technologies* **11**, 179 (2022).
- [29] M. Rössle, K. W. Kim, A. Dubroka, P. Marsik, C. N. Wang, R. Jany, C. Richter, J. Mannhart, C. W. Schneider, A. Frano, P. Wochner, Y. Lu, B. Keimer, D. K. Shukla, J. Strempler, and C. Bernhard, *Physical Review Letters* **110**, 136805 (2013).
- [30] M. Yazdi-Rizi, P. Marsik, B. P. P. Mallett, and C. Bernhard, *Physical Review B* **95**, 024105 (2017).
- [31] D. W. Berreman, *Journal of the Optical Society of America* **62**, 502 (1972).
- [32] H. G. Tompkins and E. A. Irene, eds., *Handbook Of Ellipsometry* (William Andrew, Inc, 2004).
- [33] H. G. Tompkins and E. A. Irene, eds., *Handbook of ellipsometry* (William Andrew, Inc, 2004) Chap. 7.
- [34] T. Nagashima and M. Hangyo, *Applied Physics Letters* **79**, 3917 (2001).
- [35] M. Neshat and N. P. Armitage, *Optics Express* **20**, 29063 (2012).
- [36] V. G. Veselago, *Soviet Physics Uspekhi* **10**, 509 (1968).
- [37] A. D. Boardman, N. King, and L. Velasco, *Electromagnetics* **25**, 365 (2005).
- [38] T. Dumelow and D. R. Tilley, *Journal of the Optical Society of America A* **10**, 633 (1993).
- [39] P. A. Belov, *Microwave and Optical Technology Letters* **37**, 259 (2003).
- [40] R. R. da Silva, R. M. da Silva, T. Dumelow, J. A. P. da Costa, S. B. Honorato, and A. P. Ayala, *Physical Review Letters* **105**, 163903 (2010).
- [41] R. Macêdo, R. R. da Silva, T. Dumelow, and J. da Costa, *Optics Communications* **310**, 94 (2014).
- [42] A. J. Hoffman, L. Alekseyev, S. S. Howard, K. J. Franz, D. Wasserman, V. A. Podolskiy, E. E. Narimanov, D. L. Sivco, and C. Gmachl, *Nature Materials* **6**, 946 (2007).
- [43] J. Humlíček, *Thin Solid Films* **519**, 2655 (2011).
- [44] F. Gervais and B. Piriou, *Journal of Physics C: Solid State Physics* **7**, 2374 (1974).
- [45] See Supplemental Material at [URL will be inserted by publisher] for full measured data and fitted parameters.

Appendix A: materials of "Broad-band ellipsometry study of the anisotropic dielectric response of  $\text{YAlO}_3$ "

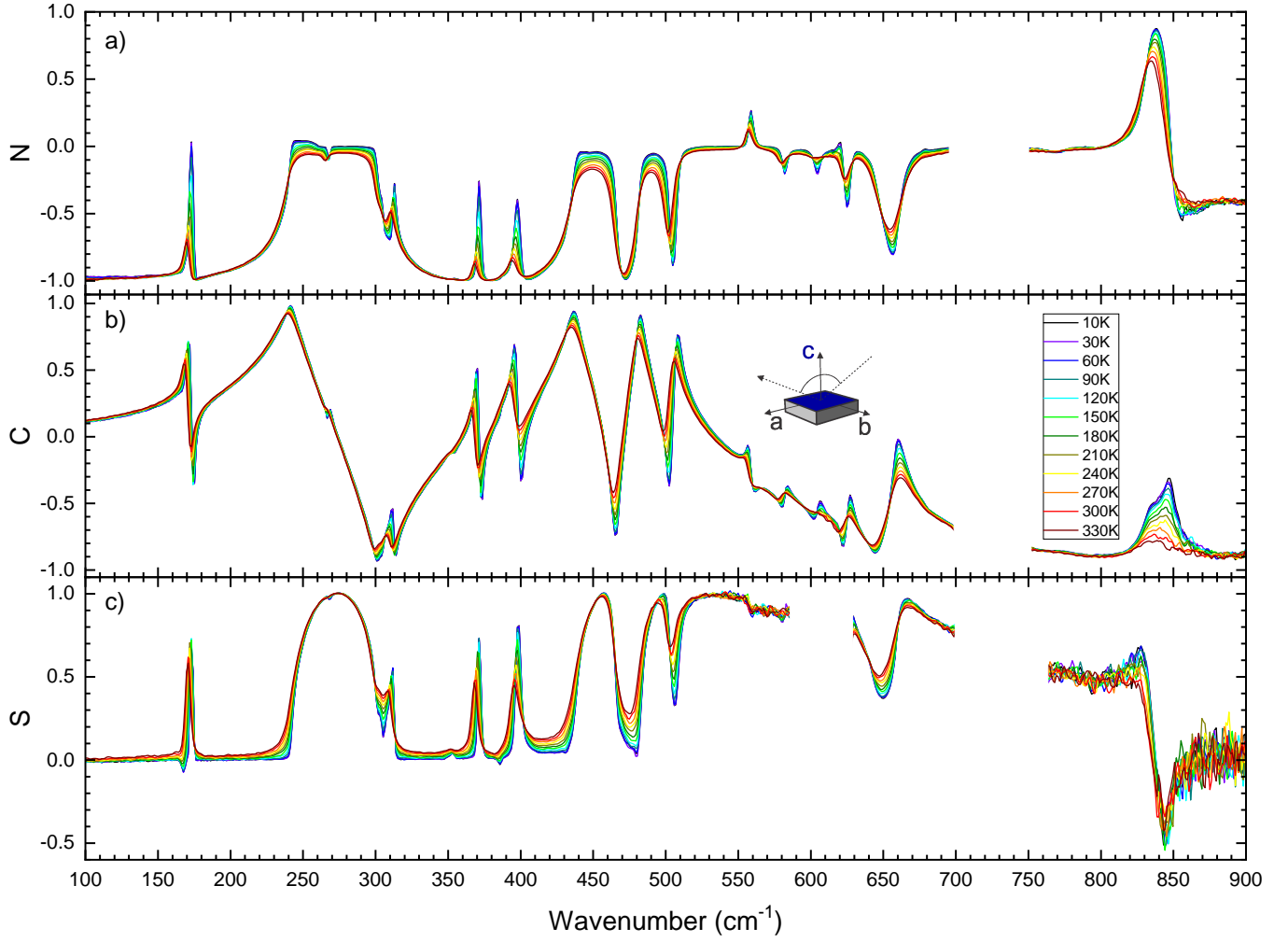


FIG. 7. FIR response along the  $a$ -axis measured on  $c$ -cut  $\text{YAlO}_3$  at angle of incidence  $\varphi = 75^\circ$ , at temperature from 10 to 330 K : in a) the  $N$  element, in b) the  $C$  element and in c) the  $S$  element of the Mueller Matrix. The polyethylene window of the detector and the polyethylene substrate of the polarizers are not transparent in the spectral region  $700$  to  $750 \text{ cm}^{-1}$ . To obtain the  $S$  data in c), we used a Si-prism as a compensator. In this case, the Si material are not transparent in the spectral region  $590$  to  $630 \text{ cm}^{-1}$ .

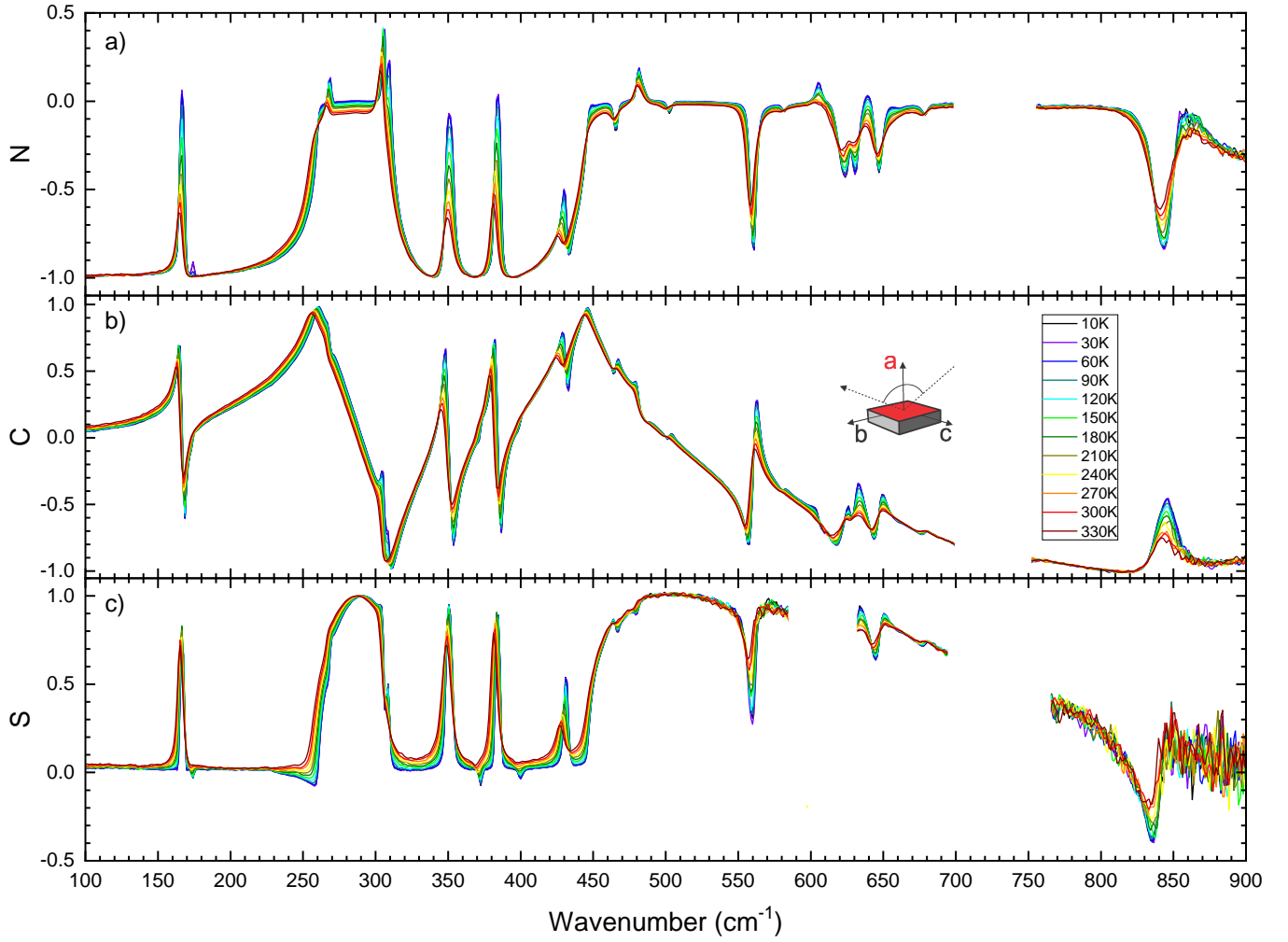


FIG. 8. FIR response along the  $b$ -axis measured on  $a$ -cut  $\text{YAlO}_3$  at angle of incidence  $\varphi = 75^\circ$ , at temperature from 10 to 330 K : in a) the  $N$  element, in b) the  $C$  element and in c) the  $S$  element of the Mueller Matrix. The polyethylene window of the detector and the polyethylene substrate of the polarizers are not transparent in the spectral region 700 to  $750 \text{ cm}^{-1}$ . To obtain the  $S$  data in c), we used a Si-prism as a compensator. In this case, the Si material are not transparent in the spectral region 590 to  $630 \text{ cm}^{-1}$ .

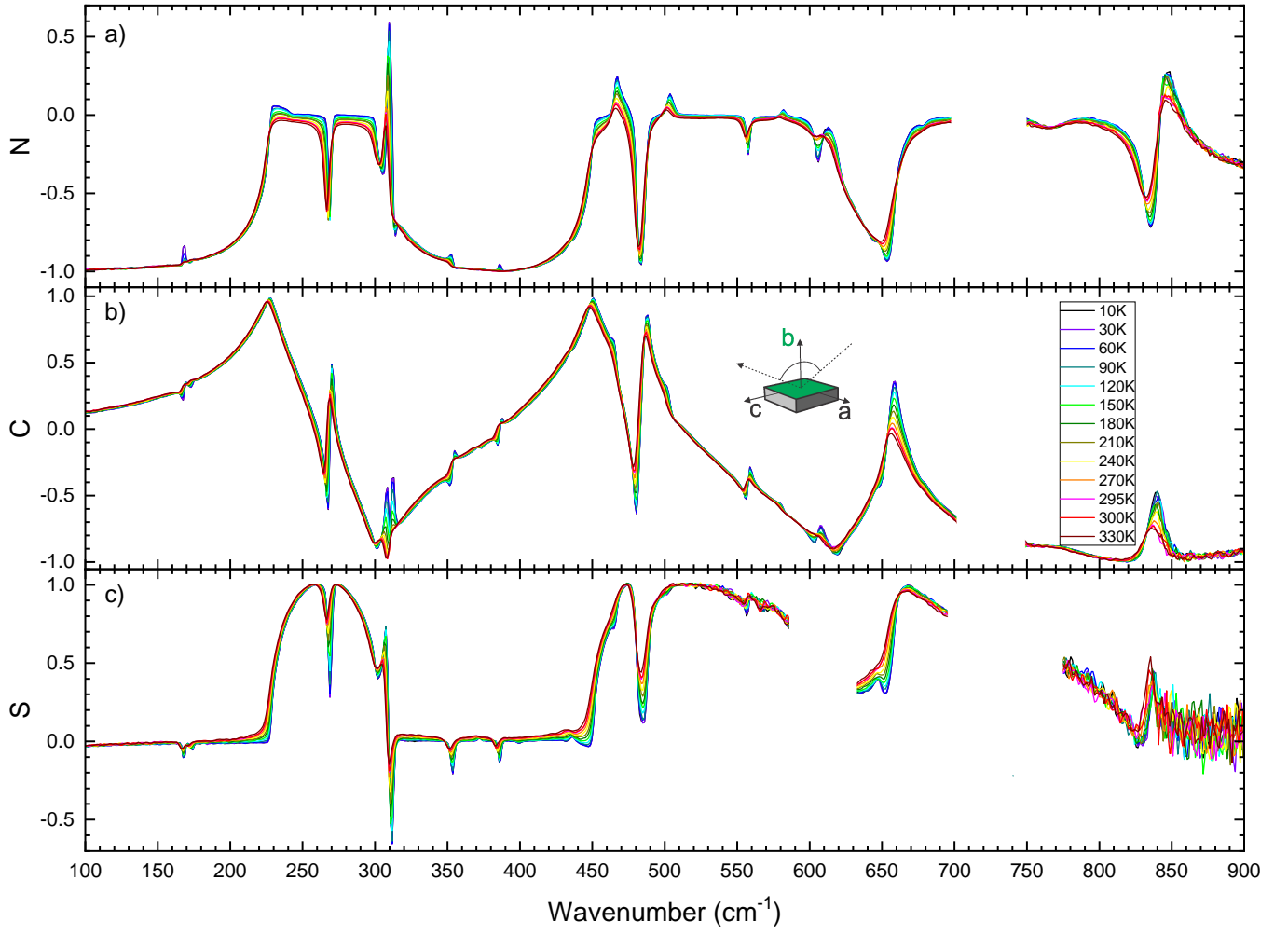


FIG. 9. FIR response along the  $c$ -axis measured on  $b$ -cut  $\text{YAlO}_3$  at angle of incidence  $\varphi = 75^\circ$ , at temperature from 10 to 330 K : in a) the  $N$  element, in b) the  $C$  element and in c) the  $S$  element of the Mueller Matrix. The polyethylene window of the detector and the polyethylene substrate of the polarizers are not transparent in the spectral region 700 to  $750 \text{ cm}^{-1}$ . To obtain the  $S$  data in c), we used a Si-prism as a compensator. In this case, the Si material are not transparent in the spectral region 590 to  $630 \text{ cm}^{-1}$ .

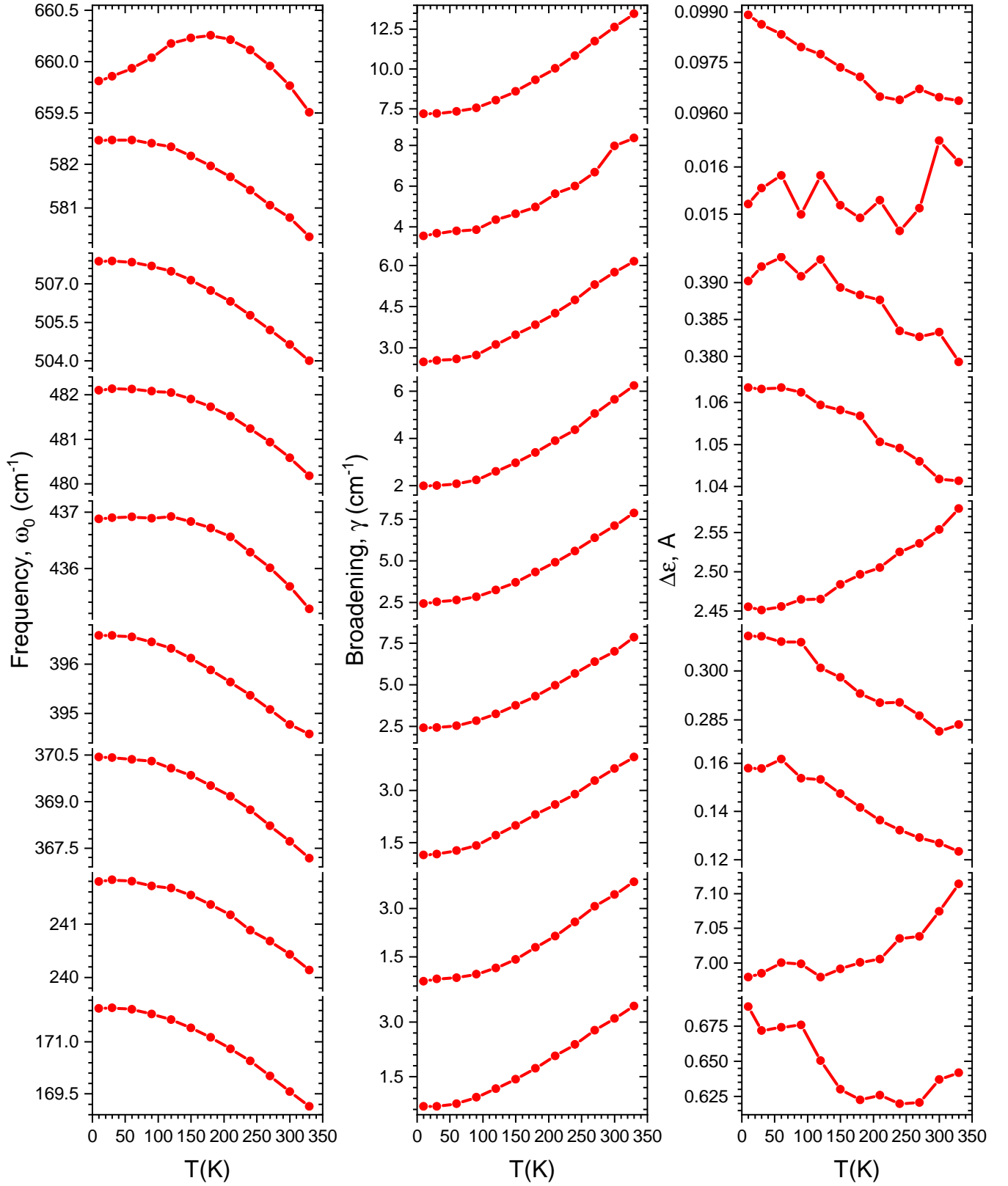


FIG. 10. Temperature dependence of  $\text{YAlO}_3$  a-axis infrared-active TO phonons in terms of eigenfrequency  $\omega_0$ , broadening  $\gamma$  and strength  $A = \Delta\varepsilon$ , at temperatures from 10 to 330 K.

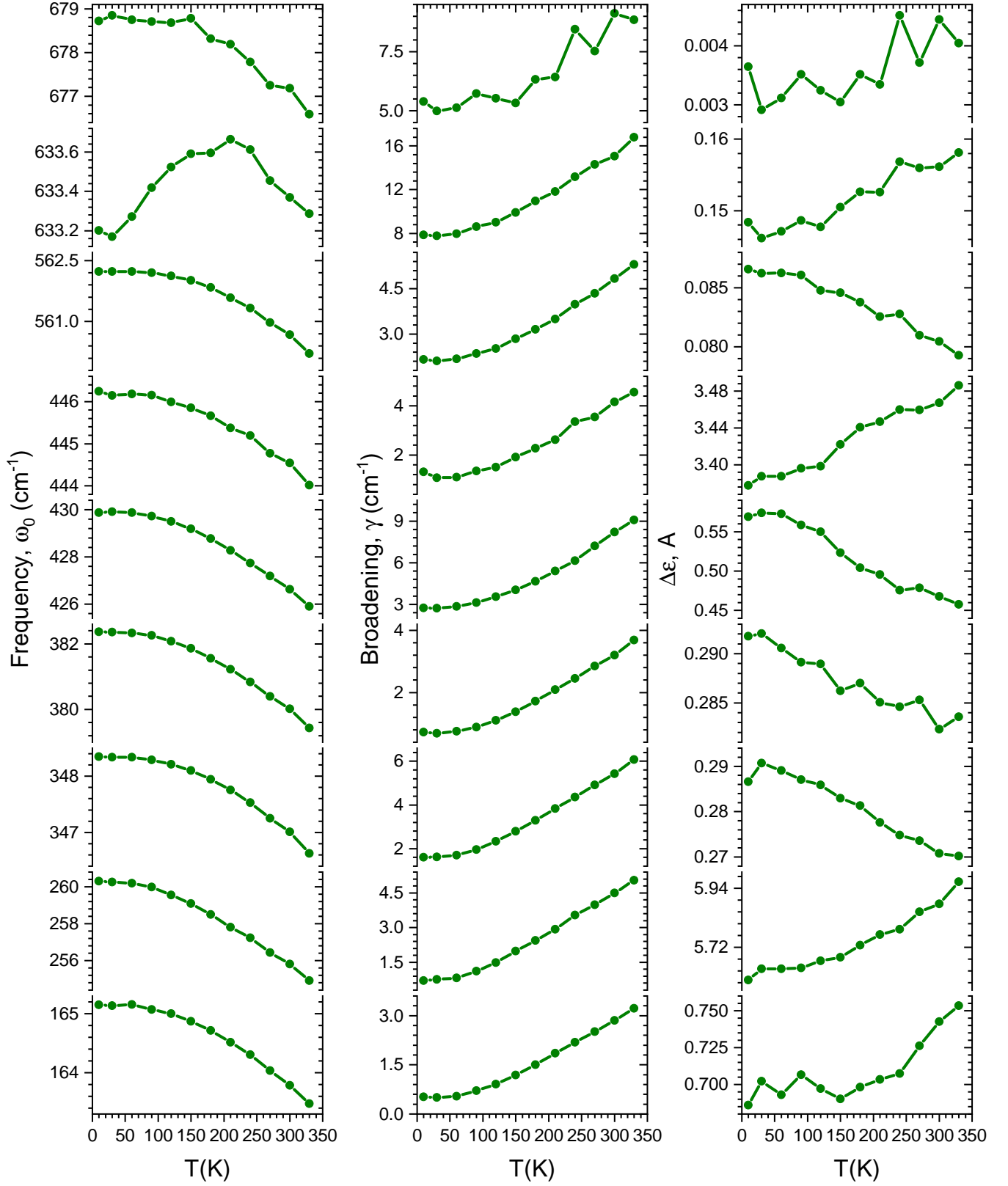


FIG. 11. Temperature dependence of  $\text{YAlO}_3$  b-axis infrared-active TO phonons in terms of eigenfrequency  $\omega_0$ , broadening  $\gamma$  and strength  $A = \Delta\varepsilon$ , at temperatures from 10 to 330 K.

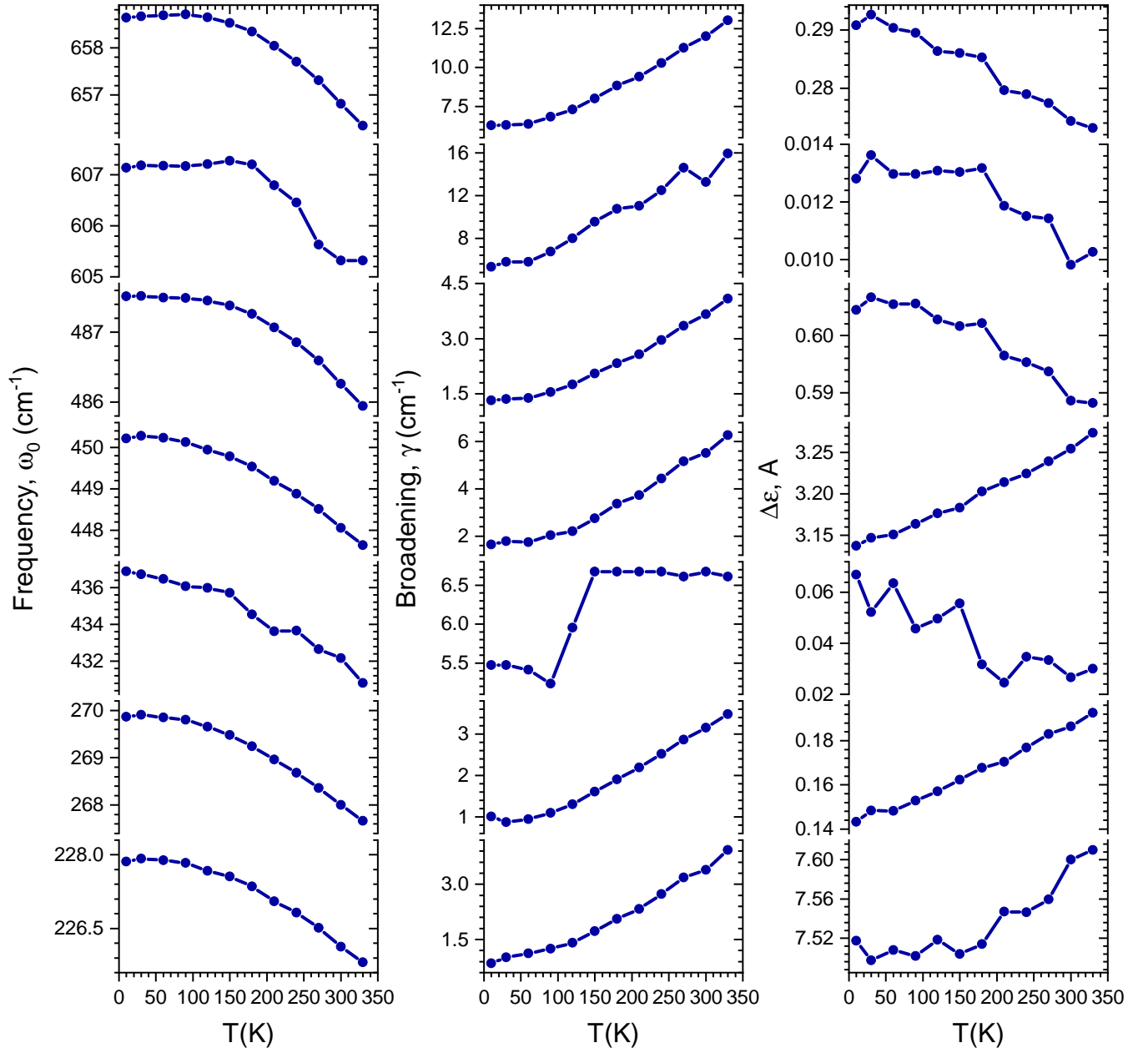


FIG. 12. Temperature dependence of YAIO<sub>3</sub> c-axis infrared-active TO phonons in terms of eigenfrequency  $\omega_0$ , broadening  $\gamma$  and strength  $A = \Delta\epsilon$ , at temperatures from 10 to 330 K.